Title: Dysregulation of macrophage lipid metabolism underlies intracellular bacterial neuroinvasion

Authors: Zhou Sha[1, #], Kun Yang[2, #], Shoupeng Fu[3, #], Xiaoyong Tong[4, #], Hui Yang[1], Huiling Fang[1], Qianqian He[1], Ning Li[5, 6], Xinyu Shu[5, 6], Qi Liu[1], Yongliang Du[1], Beibei Fu[1], Yan Xiong[1], Dong Guo[1], Jing Liu[4], Qian Li[7], Hao Zeng[8], Xiaokai Zhang[8], Rui Yao[9], Xushuo Zhang[10], Wenjin Guo[3], Xuhu Mao[7], Mian Long[5, 6], Xiaoyuan Lin[7, 11, *], Quanming Zou[8, *], Haibo Wu[1, *]

1 School of Life Sciences, Chongqing University, Chongqing 401331, China

2 Chongqing Public Health Medical Center, Chongqing 400036, China

3 School of Veterinary Medicine, Jilin University, Changchun 130062, China

4 School of Pharmaceutical Sciences, Chongqing University, Chongqing 401331, China

5 Center of Biomechanics and Bioengineering, Key Laboratory of Microgravity (National Microgravity Laboratory), and Beijing Key Laboratory of Engineered Construction and Mechanobiology, Institute of Mechanics, Chinese Academy of Sciences, Beijing 100190, China

6 School of Engineering Sciences, University of Chinese Academy of Sciences, Beijing 100049, China

7 Department of Clinical Microbiology and Immunology, College of Pharmacy and Laboratory Medicine, Army Medical University (Third Military Medical University),

Chongqing 400038, China.

8 National Engineering Research Center of Immunological, Department of Microbiology and Biochemical Pharmacy, College of Pharmacy and Laboratory Medicine, Army Medical University (Third Military Medical University), Chongqing 400038, China.

9 Department of Pathology, Chongqing Hygeia Hospital, Chongqing 401331, China

10 Zhejiang Toyouvax Biopharming, Hangzhou 311100, China

11 Institut für Virologie, Freie Universität Berlin, Robert-von-Ostertag-Str. 7-13, Berlin 14163, Germany.

# Equally Contributing Authors

* Corresponding authors

Xiaoyuan Lin, linxiaoyuan23@163.com

Quanming Zou, qmzou2007@163.com

Haibo Wu, hbwu023@cqu.edu.cn

Abstract

Acute infection of the central nervous system is one of the deadliest diseases, but the mechanisms by which intracellular bacteria infiltrate the brain remain poorly understood. Phagocytic cells are usually recognized as the battlefield on which war is waged against intracellular bacteria; however, little is known about how the intracellular bacteria take advantage of infected phagocytes to access the brain. In this study, we find that a novel $CD36^+$ foamy macrophage subpopulation participates in penetration of the brain by intracellular bacteria. Biomechanical analysis reveals that abundant protrusions and adhesion molecules on foamy macrophages confer significant resistance to the mechanical stress of blood flow, thereby providing more opportunities for these macrophages to adhere to the vascular endothelial surface during neuroinvasion. Through metabolomics analysis, we find that macrophage lipid metabolism is recalibrated during bacterial neuroinvasion, and that β-hydroxybutyrate promotes the formation and survival of $CD36^+$ foamy macrophages. Taken together, our findings uncover a pathway by which intracellular bacteria hijack macrophages to invade the brain, suggesting that lipid metabolism might play a role in the prevention or resolution of bacterial neuroinvasion.

Keywords: intracellular bacteria; neuroinvasion; foamy macrophage; ketogenesis; β-hydroxybutyrate

Introduction

Meningitis is an inflammation of the protective membranes covering the brain that caused by bacterial or viral infection.[1,2] The meninges consist of multiple layers of membranes that protect the central nervous system from injury and infection.[3,4] Some intracellular bacteria, including *Salmonella typhimurium* (*S. typhimurium*) and *Mycobacterium tuberculosis* (*M. tuberculosis*), can invade the meninges to cause severe brain pathology.[5-7] Bacterial meningitis is a life-threatening infection with extremely high mortality; however, the mechanism by which bacteria invade the brain remains unclear. Efforts to understand the factors that promote neuroinvasion and host responses to these pathogens are urgently needed.

Phagocytes, such as neutrophils and macrophages, play dominant roles in host response to intracellular bacteria.[8] The primary function of phagocytes is to uptake and destroy microorganisms and cell debris through tissue circulation and migration.[9,10] Via phagocytosis and antigen presentation, phagocytes act rapidly as the first line of defense against bacterial infections. However, intracellular bacteria can employ sophisticated strategies to replicate within phagocytes and evade host immune surveillance.[11-13] Recently, Marc Lecuit et al. showed that the surface protein internalin B of *Listeria monocytogenes* (*L. monocytogenes*) protects infected monocytes from immune killing by $CD8^+$ T cells, thus prolonging the lifespan of infected cells and facilitating the spread of infection throughout the central nervous system.[13] In this context, phagocytes, especially monocytes and macrophages, might

play important roles during neuroinvasion, but exactly how intracellular bacteria take advantage of infected macrophages is not well understood.

Infectious diseases and host metabolism are closely linked. Metabolic signaling helps awaken the immune system to resist pathogenic invasion. For example, glycolysis bolsters T cell immunity to prevent *L. monocytogenes* infection.[14] In addition, many studies have shown that bacteria can actively or passively manipulate host metabolites to evade clearance by the host immune system. [11,15,16] *Ruminococcus gnavus* initiates biosynthesis of phenethylamine and tryptamine, which exacerbates the progression of diarrhea-predominant irritable bowel syndrome.[11] *Legionella pneumophila* induces Warburg-like metabolism by secreting the type 4 secretion system effector MitF and decreases oxidative phosphorylation (OXPHOS) in infected macrophages to increase the pathogen's likelihood of survival.[15] A recent report indicates that Nav1.8^{+} nociceptors send signals to meningeal macrophages via the calcitonin gene-related peptide, and this neuroimmune axis suppresses host defenses and exacerbates bacterial meningitis.[16] These findings imply a potentially close connection between host metabolism and bacterial brain invasion.

Ketogenesis, induced by fasting or dietary supplementation, is a metabolic pathway that provides an alternative form of energy for the body and is closely related to host immune response. [17,18] A recent study reports that in pneumonia caused by *Pseudomonas aeruginosa*, ketone bodies are recycled to the lungs via OXPHOS to

111 maintain airway homeostasis.[19] Consistently, a ketogenic diet is reported to activate
112 the expansion of protective γδ T cell responses against influenza virus infection.[20]
113 However, researchers have also found that pathogens can achieve intracellular
114 survival and infection progression by manipulating host ketogenesis.[21] Mice fed a
115 ketogenic diet develop a hyperinflammatory response to systemic lipopolysaccharide
116 and an increased mortality rate, phenomena that are independent of diet-induced
117 microbiota and hyperglycemia.[21] Therefore, the role of ketogenesis in the progression
118 and migration of infections is controversial.[22] β-hydroxybutyrate (BHB) produced by
119 ketogenesis is well known to promote the accumulation of intracellular lipid bodies,
120 which serve as both a source of nutrients and a secure niche for intracellular bacteria.[23]
121 However, how ketogenesis and BHB participate in regulating monocytic/macrophagic
122 homeostasis and their roles in bacterial neuroinvasion are poorly defined.
123
124 In this study, we discovered a novel subpopulation of $CD36^+$ macrophages that served
125 as immune 'Trojan horses', crossing the blood-brain barrier (BBB) and enabling
126 intracellular bacterial neuroinvasion. This macrophage subset has a foamy phenotype,
127 which improves the cells' ability to stay and migrate vertically on the cerebrovascular
128 endothelial surface under the mechanical stress of blood flow. Furthermore, we found
129 that serum BHB, which might be produced by a ketogenic diet, exacerbated bacterial
130 neuroinvasion by increasing the formation and promoting the survival of foamy
131 macrophages in peripheral blood. Our study outlines a new common strategy
132 employed by intracellular bacteria in brain invasion, which could be a potential

therapeutic target in the treatment of bacterial meningitis.

Results

CD36^{+} foamy macrophages are potential carriers of bacteria during brain invasion

To study the role of immune cells in bacterial neuroinvasion, we performed single-cell RNA-sequencing (scRNA-seq) of peripheral blood mononuclear cells (PBMCs) collected from mice in an acute meningitis model of *L. monocytogenes* infection (Figure 1A). We conducted scRNA-seq 24 hours post infection, at which timepoint bacteria had massively invaded the brain and mice began to die (Figure S1A and S1B). Immune cell lineages were identified using canonical surface markers of dendritic cells (DCs: *Xcr1, Flt3, CD209a*), NK cells (*Nkg7*), T cells (*CD3*), monocyte/macrophages (Mo/Mφ: *Fcgr1, Adgre1*), B cells (*CD79*), neutrophils (*S100a9, S100a8*; Figure 1B and 1C).[24] Among these lineages, Mo/Mφ are involved in phagocytosis and intracellular killing of microorganisms; however, intracellular bacteria can also live in these cells to achieve long-term latent infection.[25] In this case, Mo/Mφ (n=3535 cells) were extracted and reclustered *in silico* to precisely delineate subpopulations and their distributions before and after neuroinvasion. Based on differentially expressed cell surface markers and transcripts, we annotated Mo/Mφ into 6 subpopulations (Figure 1D, S1C). Results showed that the percentage of Cluster 2 cells was sharply increased in the neurolisteriosis group (Figure S1D). Further, we

found that Cluster 2 cells expressed high levels of genes related to lipid accumulation, including *CD36*, peroxisome proliferator–activated receptor gamma (*Pparg*), *CD9*, apolipoprotein E epsilon (*ApoE*), fatty-acid binding protein 4 (*Fabp4*), and triggering receptor expressed on myeloid cells 2 (*Trem2*; Figure. 1E). [26-30] These data implied that the functional role of Cluster 2 macrophages was closely related to lipid metabolism.

As previously reported, lipid accumulation in macrophages easily exceeds their homeostatic capacity, triggering lipid droplet formation and causing the macrophages to have a foamy appearance. [31,32] To understand the characteristics of Cluster 2 macrophages, $CD36^{+}$ and $CD36^{-}$ macrophages were isolated from peripheral blood by fluorescence-activated cell sorting. Compared with $CD36^{-}$ macrophages, the $CD36^{+}$ subpopulation exhibited significantly higher granularity (SSC^{hi}; Figure S1E), which indicated the number of proteins or organelles they contained and the protrusions on their surfaces. Increased granularity is considered a characteristic of foamy macrophages.[33] The sorted macrophages were cultured *in vitro* overnight and then labeled with BODIPY FL, a lipophilic probe for polar and neutral lipids. Results showed that the $CD36^{+}$ subpopulation accumulated significantly more lipid droplets than the $CD36^{-}$ macrophages (Figure S1F). We also performed Oil Red O staining to validate this finding (Figure S1F). To confirm the lipid uptake ability of the $CD36^{+}$ macrophages, we used fluorescently labeled 1,1′-dioctadecyl-3,3,3′,3′-tetramethylindocarbocyanine perchlorate (Dil)–conjugated oxidized low-density lipoprotein (oxLDL) particles and our findings showed that $CD36^{+}$ macrophages took

177 up more than twice as much ox-LDL as $CD36^{-}$ macrophages (Figure S1G). These
178 data confirmed the foamy appearance of the Cluster 2 macrophages during brain
179 invasion.
180
181 Next, we performed flow cytometry to detect percentage changes in foamy
182 macrophages over time during neurolisteriosis (Figure S1E). The results showed that
183 the percentage of $CD36^{+}$ foamy macrophages in peripheral blood steadily increased
184 over time during neuroinvasion (Figure 1F). The $CD36^{+}$ subgroup could exceed 52%
185 of all macrophages (Figure 1G). In addition, the percentage of foamy macrophages in
186 peripheral blood was positively associated with bacterial load in the brain (Figure 1H).
187 These data implied that $CD36^{+}$ foamy macrophages might be involved in bacterial
188 neuroinvasion. Furthermore, immunofluorescence co-localization analysis was used
189 to validate this hypothesis. The results showed that the number of $CD36^{+}$ foamy
190 macrophages attached to cerebrovascular endothelial cells (CVECs) increased as
191 neuroinvasion progressed in the acute meningitis model (Figure 1I). Taken together,
192 these results suggested that $CD36^{+}$ foamy macrophage might play an important role in
193 bacterial brain invasion.
194
195 **$CD36^{+}$ foamy macrophages facilitate transport of intracellular bacteria across**
196 **the blood-brain barrier**
197 Next, we sought to understand how necessary $CD36^{+}$ foamy macrophages were to
198 bacterial neuroinvasion. Using mouse primary CVECs and neurons in a Transwell

system, we constructed an *in vitro* BBB model (Figure 2A). Ox-LDL has been reported to induce foamy cell formation by enhancing CD36 expression[34]; therefore, we converted peritoneal macrophages isolated from mice into $CD36^+$ foamy macrophages by treating them with different concentrations of ox-LDL for 24 hours (Figure S2A). Subsequently, macrophages were infected with *L. monocytogenes* (MOI=10) and then inoculated in the upper Transwell chamber of the BBB model. We confirmed that intracellular bacterial load increased with the transformation of macrophages into the foamy phenotype (Figure S2B). Of note, the assistance of ox-LDL–stimulated macrophages significantly increased the number of *L. monocytogenes* organisms crossing the BBB in a dose-dependent manner (Figure 2B). Using crystal violet staining, we also demonstrated a dose-dependent increase in the number of macrophages penetrating the endothelial monolayer upon stimulation with ox-LDL (Figure 2C and 2D).

To understand whether the increase in $CD36^+$ foamy macrophages favored the transfer of *L. monocytogenes* into the brain *in vivo*, we performed adoptive macrophage transfer experiments through tail vein injection based on a cyclophosphamide (CTX)-induced immunosuppressive mouse model (Figure 2E). Consistent with previous studies, *L. monocytogene*-induced clinical phenotype and mortality were relieved in the mice transferred with purified peritoneal macrophages (PMφ group; Figure 2F, S2C and S2D).[35,36] However, body weight was reduced, comprehensive clinical scoring was increased, and survival time was shortened in the mice transferred with $CD36^+$

221 foamy macrophages compared with the control (FMφ group; Figure 2F, S2C and
222 S2D). Furthermore, we showed that brain bacterial loads in mice transferred with
223 $CD36^+$ macrophages were significantly higher than those in mice transferred with
224 purified peritoneal macrophages (Figure 2G). Interestingly, bacterial loads did not
225 differ among the lung, spleen, and liver (Figure S2E). We also tested proinflammatory
226 factor levels in plasma and brain homogenate. The results showed that levels of
227 interleukin 6 (IL-6) and tumor necrosis factor alpha (TNF-α) were remarkably
228 increased (Figure 2H and 2I), indicating a more severe phenotype of meningitis in the
229 foamy macrophage transferred group. Pathological histology analysis confirmed the
230 existence of more severe inflammation and neuronal damage in the cerebral cortices
231 in mice transferred with foamy macrophages than in those of control (Figure S2F and
232 S2G). In addition, when mice were infected with a relatively low dose (5×10^7
233 CFU/mouse) of *L. monocytogenes*, the difference in bacterial load in brain tissues
234 between foamy macrophage transferred mice and the control group was even greater
235 than that under high dose condition (Figure S2H and S2I). These data suggested that
236 neuroinvasion mediated by $CD36^+$ foamy macrophages were not restricted to an acute
237 meningitis model induced by high dose bacteria.
238
239 We then wondered whether $CD36^+$ foamy macrophages might play the same role
240 during brain invasion by other intracellular bacteria. In the relevant experiment, a
241 positive correlation between $CD36^+$ foamy macrophages and neuroinvasion was
242 observed in meningitis models of the intracellular bacterium *S. typhimurium* (Figure

S3A and S3B). We observed the same result in neuroinvasion model of Methicillin-resistant *Staphylococcus aureus* (MRSA; Figure S3C and S3D), which, although not a classical intracellular pathogen, exhibits significant intracellular habitation.[37] However, this finding was not validated in a neuroinvasion model of the extracellular bacterium *Streptococcus pneumoniae* (*S. pneumoniae*; Figure S3E and S3F). Next, we performed adoptive macrophage transfer experiments to further verify the carrier role of $CD36^+$ foamy macrophages in intracellular bacterial invasion of the brain. We again observed differences in brain tissue bacterial loads between the foamy macrophage transferred and control groups in the meningitis models of MRSA (Fig. S3G-S3K), but not in models using *S. pneumoniae* (Figure S3L-S3O). Taken together, these data suggested that $CD36^+$ foamy macrophages greatly contributed to the process of intracellular bacterial neuroinvasion.

Proprotein convertase subtilisin/kexin 9 (PCSK9) belongs to the proprotein convertase family, whose members participate in cholesterol and fatty acid (FA) metabolism. [38,39] Intracellular low-density lipoprotein cholesterol (LDL-C) accumulates because LDL receptor located on the cell membrane cannot be degraded normally in $PCSK9^{-/-}$ mice.[40,41] We found that PCSK9-deficient macrophages had significantly higher lipid content compared with control (Figure S4A and S4B) and that more *L. monocytogene* organisms parasitized $PCSK9^{-/-}$ macrophages than they parasitized wild-type (WT) cells (Figure S4C). During neurolisteriosis, $PCSK9^{-/-}$ mice had higher percentages of $CD36^+$ foamy macrophages in peritoneal blood than their

littermates (Figure S4D). Therefore, we used PCSK9$^{-/-}$ mice as a model of spontaneously forming foamy macrophages, and verified the reliability of our findings through adoptive macrophages transfer. After recovery from transfer for 12 hours, recipient mice were intraperitoneally injected with 2×10^8 CFU of *L. monocytogenes*; 12 h later, samples were collected for further examinations (Figure 2J). We found that brain bacterial loads were significantly higher in PCSK9$^{+/+}$ recipients that had been transferred with PCSK9$^{-/-}$macrophages than in those that had received WT macrophages (Figure 2K). Similar results were observed in the PCSK9$^{-/-}$ recipients (Figure 2K). However, differences in bacterial load manifested in brain tissues only, not in other organs such as the lung, spleen, and liver (Figure S4E). Consistently, the mortality rate, and pro-inflammatory factors in the plasma and brain homogenate were aggravated in both PCSK9$^{+/+}$ and PCSK9$^{-/-}$ recipients by transfer of PCSK9$^{-/-}$ macrophages (Figure 2L, S4F and S4G). Since *L. monocytogene* is a foodborne pathogen that can invade the body through the gastrointestinal tract, we further confirmed the above-mentioned finding by oral administration of *L. monocytogenes* in the same experimental model (Figure 2M and 2N, S4H-S4J). Taken together, these data indicated that excess lipid accumulation contributed to the foamy appearance of macrophages, thereby facilitating neuroinvasion by intracellular bacteria.

Shear flow analysis demonstrates increased adhesion and resistance of foamy macrophages during neuroinvasion

287 We next asked how CD36$^+$ foamy macrophages exploited their properties to
288 accumulate on the cerebral blood vessel wall and participate in the process of
289 intracellular bacterial neuroinvasion. Using a two-dimensional live-cell flow chamber
290 assay with a microfluidic chip[42], we deciphered the multistep process of how
291 macrophages adhered to and moved on the surface of vascular endothelium under
292 physiological flow (Figure 3A). Cellular adhesion ability was calculated by counting
293 total macrophages adhering to the endothelial monolayer under a given shear stress.
294 We found that as the percentage of CD36$^+$ foamy macrophages increased, so did the
295 number of cells adhering to the endothelial monolayer (Figure 3B and 3C). Because
296 adherent cells could be detached by an increase in shear stress, we tested the
297 dynamics of CD36$^+$ foamy macrophages' shear resistance. The results showed that
298 such resistance was significantly stronger than that of control macrophages: CD36$^+$
299 foamy macrophages outstandingly resisted high shear stress (Figure 3D). Further, we
300 investigated the effect of endothelial density on macrophagic adhesion. Results
301 showed that endothelial cell density, rather than cell type, greatly affected
302 macrophagic adhesion, and foamy macrophages tended to adhere to the surface of
303 dense endothelial cells (Figure S5A-S5D).
304
305 Once attached to the endothelial monolayer, the macrophage crawls along it and finds
306 a place to cross it in the presence of blood flow. [43,44] We next tested the performance of
307 CD36$^+$ foamy macrophages in post-arrest crawling on the endothelial monolayer. We
308 acquired sequential images of macrophages at a shear stress of 2 dyn/cm^2 and then

analyzed them by defining various parameters of crawling dynamics (Figure S5E). The observations were presented by crawling trajectories of each individual cells (Figure 3E), and we found that the crawling ability of adherent $CD36^+$ foamy macrophages was dampened, reflecting in shortened crawling displacement and slower crawling speed (Figure 3F and 3G). However, we saw no obvious differences in crawling duration (Figure S5F). Directionality is also a critical aspect of cell crawling dynamics, it is quantified as the ratio of displacement along shear flow to the perpendicular. Our results showed that the directionality of macrophages was slightly but significantly enhanced by ox-LDL stimulation, implying that macrophagic foaminess tended to drive cell crawling in the vertical direction (Figure 3H). We also compared a key dynamic parameter of transmigration duration, which is defined as the interval from the timepoint of cell arrival at the site to the endpoint of completion of transmigration beneath the endothelial monolayer (Figure S5G). The result showed that transmigration duration was significantly shortened in $CD36^+$ foamy macrophage (Figure 3I).

Considering that protrusion is critical for cell crawling and migration, we then investigated whether intercellular lipid could affect the formation of protrusions. The results showed that the numbers, as well as the lengths of protrusions were significantly increased in $CD36^+$ foamy macrophages (Figure 3J and 3K). We further quantified macrophagic cell area and found that the mean area of foamy macrophages was significantly larger than the control (Figure 3L). Additionally, we examined

various integrins and adhesive ligands expressed on the cell surface, which have been reported to be involved in adhesion and migration.[45] The results showed that the expression levels of α-integrins, β-integrins and intercellular adhesion molecules were significantly upregulated in the infected $CD36^+$ foamy macrophages (Figure 3M). Collectively, these data suggested that the foaminess of macrophages greatly enhanced their ability to adhere under mechanical stress, predisposing them to stay and to migrate vertically on the surface of CVECs; this might be attributable to the formation of protrusions as well as the expression of integrins and adhesion ligands.

β-hydroxybutyrate promotes foamy macrophage formation and exacerbates neuroinvasion

Having shown foamy appearance to be closely linked to the excess lipid accumulation in macrophages, we performed lipid metabolomics analysis of serum samples to reveal how foamy macrophages were formed during bacterial neuroinvasion. Principal component analysis (PCA) showed that distinct metabolite genotype clusters were generated in the neurolisteriosis group (Figure 4A). The volcano plot indicated that 70 FAs were upregulated and 71 FAs were downregulated ($p < 0.05$, $|\log_2(\text{fold change})| > 1$) in the neurolisteriosis group (Figure 4B, Table S1). The 70 upregulated FAs were classified into four subclusters by the number of carbon atoms in the alkyl chain. We found that BHB, which has been reported to favor the foamy phenotype of macrophages [46], was the only short-chain FA among all upregulated FAs (Figure 4C). KEGG-based analysis revealed that metabolites related to the synthesis and

degradation of ketone bodies were enriched (Figure S6A), and metabolomics data showed that BHB was significantly increased during neuroinvasion (Figure S6B). Based on these data, we detected serum BHB level in the acute meningitis model of *L. monocytogenes* infection. The results showed that BHB level climbed steadily over time and then decreased slightly (Figure 4D). Consistently, an upregulation of genes controlling ketogenic enzymes (HMGCS2 and CPT1A) in the liver was observed as infection persisted (Figure S6C and S6D). Meanwhile, mice experienced weight loss and decreased appetite during the experiments, which was partly related to enhanced ketogenic ability after infection (Figure S6E and S6F). Furthermore, a steady increase of serum BHB was also observed in the meningitis models established using *S. typhimurium* and MRSA (Figure S6G and S6H). These data confirmed that production of BHB was significantly induced during bacterial neuroinvasion.

As previously reported, BHB promotes the foamy phenotype of macrophages via the hydroxycarboxylic acid receptor 2 (HCAR2).[23] Therefore, we next used HCAR2 knockout mice to study whether BHB could promote bacterial neuroinvasion. We confirmed that lipid accumulation and percentage of $CD36^{+}$ macrophages all increased dramatically upon BHB stimulation, and there was no significant difference when HCAR2 was knocked out (Figure 4E-4G). BHB inhibits adenylyl cyclase activity through the HCAR2 receptor and reduces cellular cyclic adenosine monophosphate (cAMP) levels, thereby protecting lipid droplets from lipolysis by hormone-sensitive lipases.[23] As a result, we found that cAMP pretreatment eliminated

the increase in lipid content and intercellular bacterial burden stimulated by BHB; however, this phenomenon was not found in HCAR2-deficient macrophages (Figure S6I and S6J). By using the *in vitro* BBB model (Figure 2A), the number of bacteria crossing the barrier increased significantly in response to BHB stimulation in controls, but not in HCAR2$^{-/-}$ macrophages (Figure 4H). Next, peritoneal macrophages from HCAR2$^{+/+}$ and HCAR2$^{-/-}$ mice were isolated to further assess the effects of BHB on the biophysical dynamics of macrophages. The data demonstrated that BHB significantly altered the static or shear-resistant adhesion of control macrophages, but not of HCAR2$^{-/-}$ macrophages (Figure 4I-4K). We also found that BHB greatly impaired the crawling ability, including shortened crawling displacement, slowed down crawling speed and unpredictable directionality of macrophages (Figure 4L-4O). In addition, the transmigratory ability of macrophages was significantly increased when cells were pretreated with BHB (Figure 4P). Consistently, the expression levels of the α-integrin family were significantly upregulated by BHB treatment in controls, but not in HCAR2-deficient macrophages (Figure 4Q). Taken together, these data indicated that BHB facilitated the foamy phenotype of macrophages through the HCAR2 receptor, thereby affecting the process of bacterial neuroinvasion.

β-hydroxybutyrate promotes the survival of macrophages via HCAR2-mediated calcium influx

Because the foamy stage appears to be a terminal point of macrophage differentiation [47], we wondered whether, in addition to converting peritoneal macrophages to the

397 foamy phenotype, cell survival also contributed to the increase in absolute quantity of
398 foamy macrophages induced by BHB treatment. The results showed that the lactate
399 dehydrogenase (LDH) activity in the culture medium was significantly reduced in
400 response to BHB treatment, indicating a decrease in cell death (Figure 5A). Propidium
401 iodide (PI) staining was used to evaluate the membrane integrity of infected
402 macrophages, and we found that the proportion of PI^+ cells decreased from 59.7% to
403 24.5% under BHB stimulation, with no significant difference in cell viability between
404 the BHB treatment and control groups when HCAR2 was knocked out (Figure 5B and
405 5C). Calcium influx is generally recognized as a signal that triggers cell membrane
406 repair.[48] To investigate the impact of BHB-HCAR2 signaling on cytosolic calcium
407 concentration, infected macrophages were loaded with Fluo-4 AM, a fluorescent Ca^{2+}
408 indicator. The results showed that BHB induced remarkable accumulation of
409 intracellular calcium, and HCAR2 knockdown eliminated calcium influx in
410 macrophages (Figure 5D). Pretreatment of macrophages with BAPTA, a Ca^{2+} chelator,
411 reversed the BHB-induced increase in cell survival (Figure 5E and 5F). Further, we
412 tested whether calcium flux was associated with foamy macrophage-mediated
413 intracellular bacterial penetration of the BBB. As a result, inhibition of calcium flux
414 had no effect on bacterial uptake by macrophages in the upper chamber (Figure S7A);
415 however, we observed differences in bacterial loads in the macrophages that had
416 crossed the barrier (Figure 5G).
417
418 We next investigated how BHB maintained the survival of foamy macrophages. As

419 previously reported, calcium influx initiates membrane repair mainly through
420 recruitment of the endosomal sorting complexes required for transport (ESCRT)
421 machinery.[49] Our data showed that BHB treatment significantly increased the number
422 of puncta that were positive for charged multivesicular body protein 4B (CHMP4B),
423 which indicated assembly of ESCRT in the infected macrophages; HCAR2
424 knockdown or BAPTA treatment could block this membrane repair process (Figure
425 5H and 5I, S7B and S7C).Cellular membrane repair also relies on lysosomes, which
426 can rapidly fuse with the plasma membrane when intracellular Ca^{2+} concentration
427 rises. Therefore, we examined lysosomal exocytosis in the infected macrophages
428 using exofacial lysosomal-associated membrane protein 1 (LAMP1) and the release of
429 lysosomal enzymes, such as acid phosphatase (ACP), β-galactosidase (β-gal) and β-
430 hexosaminidase (β-hex). The results confirmed that BHB promoted the lysosomal
431 exocytosis in infected macrophages through the HCAR2 receptor (Figure 5J-5L, S6D-
432 S6F). These data collectively indicated that BHB signaling activated Ca^{2+}-mediated
433 membrane repair, thereby maintaining the survival of foamy macrophages via the
434 HCAR2 receptor.
435
436 **Ketogenesis exacerbates intracellular bacterial neuroinvasion**
437 BHB can be synthesized via the metabolism of FAs and ketogenesis.[50] To understand
438 the relationship between ketogenesis and bacterial meningitis, we gave mice different
439 doses of ketone ester drink for 4 weeks, and then infected them with *L.*
440 *monocytogenes* via intraperitoneal injection (Figure 6A). The data showed that ketone

ester elevated the levels of serum BHB and the proportion of foamy macrophages in peritoneal blood (Figure 6B and S8A), accompanied by remarkable increases in the clinical scores, mortality rate and bacterial load in brain tissues (Figure 6C and 6D, S8B). Dietary modulation can increase and maintain circulating metabolites in human circulation, and a growing amount of evidence demonstrates that a ketogenic diet elevates BHB levels.[51] The ketogenic diet is a low-carb, high-fat diet that causes weight loss and provides numerous health benefits, including alleviating symptoms of neurodegenerative diseases, cardiovascular diseases, and cancers.[52-55] We next asked whether a ketogenic diet was associated with neurolisteriosis. HCAR2$^{-/-}$ mice and their littermates were fed a normal or ketogenic diet for 4 weeks respectively, and then infected with *L. monocytogenes* by intraperitoneally injection (Figure 6E). As a result, the lifespan of HCAR2$^{+/+}$ mice fed a ketogenic diet was significantly shortened under *L. monocytogenes* infection, and the survival disadvantage caused by dietary modulation was abrogated by HCAR2 knockout (Figure 6F). Consistently, the clinical scores (Figure. S8C), percentages of foamy macrophages in peritoneal blood (Figure 6G), the intracellular bacterial burden of macrophages (Figure 6H), and bacterial loads in brain tissue (Figure 6I) were all greatly increased in HCAR2$^{+/+}$ mice on a ketogenic diet. Interestingly, mice in this group lost less weight than mice in the control group, and experienced greater spread of bacteria to other organs (Figure 6I and S8D). We then examined the levels of pro-inflammatory factors in the plasma and brain homogenate. The results showed that a ketogenic diet significantly increased the levels of pro-inflammatory cytokines and induced more severe neuronal damage in

463 HCAR2$^{+/+}$ mice, while it had no effect on HCAR2$^{-/-}$ mice (Figure 6J-6M). These data
464 were confirmed by oral administration of *L. monocytogenes* in the same experimental
465 model (Figure S8E-S8H). We also used MRSA to further verify our findings. The data
466 indicated that, as expected, the ketogenic diet promoted brain invasion by MRSA and
467 exacerbated symptoms of meningitis (Figure S8I-S8K). Taken together, our data
468 showed that a ketogenic diet could exacerbate bacterial neuroinvasion and hasten the
469 demise of mice, primarily depending on elevations in serum BHB via the HCAR2
470 receptor.
471
472 **Serum β-hydroxybutyrate fuels the symptoms of human bacterial meningitis**
473 Our data thus far suggested that BHB-induced CD36^{+} foamy macrophages played an
474 important role in bacterial neuroinvasion in mice. Next, we sought to assess whether
475 the accumulation of foamy macrophages or BHB could also be identified and were
476 associated with bacterial meningitis in human samples. Gender- and age-matched
477 bacterial meningitis subjects (n=62) and healthy individuals (n=60) were recruited
478 and peripheral blood samples were collected for analysis (Figure 7A). We observed no
479 significant differences in blood glucose or insulin concentrations between the two
480 groups (Figure S9A and S9C), nor was there any correlation between these parameters
481 and BHB levels (Figure S9B and S9D), excluding the involvement of glucose and
482 insulin in the differential production of BHB. As a result, serum BHB levels were
483 significantly elevated in meningitis patients compared with healthy controls,
484 suggesting an infection-induced ketogenesis (Figure 7B). Interestingly, serum

485 cholesterol levels, including total cholesterol (TC) and LDL-C were increased in
486 meningitis patients compared with healthy controls, while high-density lipoprotein
487 cholesterol (HDL-C) was slightly but not significant reduced (Figure S9E-S9G). To
488 investigate whether BHB was associated the severity of infection, we further divided
489 patients into three groups, high BHB (in the top 1/3 among samples tested, n=21),
490 moderate (middle 1/3, n=20) and low (bottom 1/3, n=21; Figure 7A). Clearly, patients
491 with high BHB levels exhibited higher clinical scores than patients with low BHB
492 levels (Figure 7C). Consistently, high-BHB patients had higher cell counts and more
493 protein in the cerebrospinal fluid (CSF; Figure 7D and 7E); higher infection indices
494 such as white blood cell counts (WBC; Figure 7F) and procalcitonin (PCT; Figure
495 7G); and higher values for markers of inflammatory conditions such as erythrocyte
496 sedimentation rate (ESR; Figure 7H) and C-reactive protein (CRP; Figure 7I),
497 suggesting increased disease severity. These data implied that infection-induced
498 ketogenesis might provide important fuel for severe bacterial neuroinvasion.
499
500 To explore the dynamics of $CD36^+$ foamy macrophages and BHB in the pathogenesis
501 of bacterial meningitis, we followed-up with 7 individuals during their hospitalization.
502 We found that $CD36^+$ foamy macrophages and BHB levels in patients tended to
503 increase during disease progression, and decrease during the recovery stage (Figure 7J
504 and 7K). To further confirm the relationship between foamy macrophages and
505 bacterial meningitis pathology, we collected PBMCs from patients or healthy controls
506 for analysis. Compared with healthy controls, the expression levels of genes involved

in cholesterol uptake were significantly increased, while those of genes related to cholesterol utilization and excretion were decreased in macrophages from meningitis patients (Figure 7L). Taken together, these data indicated that BHB fueled human bacterial meningitis by promoting the development of $CD36^+$ foamy macrophages.

Discussion

Our findings suggested that $CD36^+$ foamy macrophages might serve as carriers for intracellular bacteria that colonize in the brain, facilitating the penetration of these bacteria across the BBB. Also, we found that BHB level increased significantly in the peripheral blood of meningitis patients. Mechanistically, BHB regulated the dynamics of and morphological changes to foamy macrophages and promoted cell survival by activating the HCAR2 receptor, which is shown here to be a key signaling molecule for intracellular bacterial neuroinvasion. Furthermore, under ketogenic diet conditions, elevated BHB levels promoted the formation of foamy macrophages, thereby exacerbating bacterial transport to the brain.

Normally, the BBB prevents bacteria or viruses from crossing unless there is significant trauma to the brain. However, specific bacteria can penetrate the BBB via their unique mechanisms and cause severe brain infections.[1,13] For example, *S. pneumoniae* co-localizes with polymeric immunoglobulin receptor (pIgR) and platelet endothelial cell adhesion molecule (PECAM), leading to brain invasion.[56] *Streptococcus agalactiae* enhances the production of pro-inflammatory cytokines and

intercellular adhesion molecule-1(ICAM-1) by endothelial cells via activation of the inducible nitric oxide synthase (iNOS) pathway, resulting in direct BBB disruption.[1] Among intracellular bacteria, internalin B of *L. monocytogenes* is reported to protect infected monocytes from Fas-mediated cell killing by $CD8^+$ T cells and prolong their life-span[13]; while *M. tuberculosis* might utilize leucine-responsive regulatory protein (Lrp) to inhibit the production of pro-inflammatory cytokines, thereby promoting their survival and neuroinvasion.[57] In this context, it is likely that intracellular bacteria use the host's cells, especially immune cells, to achieve brain invasion. In this study, we discovered that $CD36^+$ foamy macrophages could be hijacked by intracellular bacteria and serve as vehicles for neuroinvasion. Compared with peritoneal macrophages, foamy macrophages tend to have more protrusions and greater cell area, which make them more conducive to colonization on CVECs under the pressure of blood flow.

Pathogens can exploit most of the host's nutrients, including glucose, glycerol, FAs, N-acetylglucosamine (GlcNAc), and several other carbon substances, for invasive transmission.[58] The T3SS effector SopE2 of *S. Typhimurium* utilizes accumulated glycolytic intermediates as carbon sources, leading to intracellular replication and pathogenicity.[59] Our findings demonstrated that intracellular bacteria can actively influence host free FA metabolism (Figure 4A-4C) and reprogram macrophages, thereby exacerbating neuroinvasion. Foamy macrophages are formed through dysregulation of lipid metabolism, and foamy phenotype impairs the immune function of macrophages and contributes to pathogenesis. For example, foamy macrophages

play a key role in the initiation, progression, and instability of atherosclerosis.[60,61] In multiple sclerosis, myelin-laden foamy macrophages in brain lesions are associated with demyelinating activity and chronic active lesions.[62] During tuberculosis, foamy macrophage necrosis expands tuberculous lesions in lung parenchyma, causing progressive destruction of lung tissue and loss of lung function in patients with active disease.[63] In this study, we discovered that BHB produced from ketogenic diets promoted the formation of $CD36^+$ foamy macrophages in peripheral blood, thereby facilitating bacterial neuroinvasion. Interestingly, we found that serum cholesterol levels, including TC and LDL-C were significantly higher in meningitis patients than in healthy controls (Figure S9E and S9G). We hypothesize that cholesterol or other lipid metabolites might also contribute to the formation of $CD36^+$ foamy macrophages. However, this hypothesis should be further verified experimentally.

Our biomechanical data indicated that $CD36^+$ foamy macrophages adhered more strongly to the endothelial surface than normal macrophages, and that this adhesion-enhancing effect was more pronounced when endothelial cells were dense (Figure 3B and 3C, S5A and S5B). This suggested that foamy macrophage-mediated bacterial invasion affected the brain to a greater extent than other tissues. Accordingly, we showed that the increase in $CD36^+$ foamy macrophages in peripheral blood led to the transfer of bacteria mainly to the brain, rather than to other organs (Figure 2G and S2E). However, we found that a ketogenic diet and ketone ester supplementation significantly increased bacterial load not only in the brain, but also in other tissues

such as the liver and lung (Figure 6D and 6I). This suggested that ketogenesis, in addition to promoting the generation of foamy macrophage, might play other unknown roles in the intracellular bacterial infections. Therefore, the role of ketogenesis in the formation of $CD36^+$ foamy macrophages and the contribution of ketogenesis to bacterial neuroinvasion should be further determined.

Host basal metabolic status may also greatly influence bacterial neuroinvasion by modifying immune cells. A previous study found that cardiac endothelial cells can oxidize ketone bodies and promote cell proliferation, migration, and blood vessel sprouting.[64] Increasing ketone body levels with a ketogenic diet increased endothelial cell proliferation and prevented vascular rarefication in a hypertrophied mouse model.[64] Whether ketogenesis directly affects the development or permeability of the BBB, leading to an increase in bacterial invasion, is unclear. Meanwhile, our study found that mice experienced weight loss and decreased appetite during the experiments (Figure S6E and S6F). Therefore, we currently cannot determine whether the elevated BHB levels were caused directly by pathogenic bacteria or by hepatic ketogenesis.

This study demonstrated that a BHB-rich environment created by the ketogenic diet rendered mice more susceptible to *L. monocytogene*-induced neuroinvasion. Mechanistically, BHB protected $CD36^+$ foamy macrophages from senescence via HCAR2-mediated membrane repair. However, inhibition of HCAR2 signaling or

calcium influx reversed the improvement in foamy macrophage survival but did not completely reverse the exacerbation in bacterial neuroinvasion induced by BHB (Figure 5E-5G). These data suggested that BHB-induced bacterial brain invasion was not solely dependent on HCAR2 signaling but that other potential mechanisms might also be involved in this process. However, this hypothesis requires further experimental verification.

Acknowledgments

This work was supported by the National Natural Science Foundation of China (No. 92369115), the Fundamental Research Funds for the Central Universities (No. 2023CDJXY-009 and 2019CDYGZD009), Natural Science Foundation of Chongqing, China (No. CSTB2023NSCQMSX0402), and Chongqing Talents: Exceptional Young Talents Project (No. cstc2021ycjh-bgzxm0099). The funders had no role in study design, data collection and analysis, decision to publish, or preparation of the manuscript.

Author Contributions

H.W., Q.Z., X.L. and Z.S. conceived and designed the study. Z.S., H.Y., H.F., Q.H., B.F., Y.X. and D.G. performed the animal experiments. Z.S., K.Y., Q.H., Q.L., Y.D. and Xushuo Z. carried out healthy volunteer and patient recruitment and sample collection. Z.S., N.L. and X.S. carried out the live-cell flow chamber assays. H.W.,

Z.S., K.Y., H.Y. and Xiaokai Z. collected and analyzed the data. X.T., S.F., J. L., R.Y., W.G., X.M. and M.L. contributed to experimental material and insightful suggestions. H.W., X.L., Xushuo Z. and Z.S. wrote the manuscript. H.W. and Q.Z. coordinated the project. All authors read and approved the final manuscript.

Declaration of interests

The authors declare no competing interests.

Figure Legends

Figure 1. Identification of CD36^{+} foamy macrophage accumulation during neurolisteriosis.

(A) Summary of experimental design (n=5 control mice and n=7 mice infected with 2×10^{8} CFU *L. monocytogenes* for 24 hours).

(B) Uniform Manifold Approximation and Projection (UMAP) representation of integrated transcriptome-based clustering. A total of 17351 peripheral blood mononuclear cells (PBMCs) were clustered and major immune cell lineages were identified.

(C) Dot plot showing the expression of selected transcripts in immune cell clusters. All transcripts were significantly enriched in the pertinent clusters with adjusted $p < 0.05$.

(D) A t-distributed Stochastic Neighbor Embedding (tSNE) analysis of the re-

clustered cells corresponding to monocytes and macrophages (baseline, n=1804; neurolisteriosis, n=1731).

(E) Expression of the indicated transcripts (encoding genes associated with lipid accumulation) was projected onto a monocyte/macrophage tSNE plot.

(F-G) An acute mouse neurolisteriosis model was generated by intraperitoneal injection of 2×10^8 CFU *L. monocytogenes.* Quantification of $CD36^+$ foamy macrophages in PBMCs (F) and total macrophages (G) was detected by flow cytometry (n=5 for each group). Experiments were performed in duplicate. Data are presented as mean ± SEM. $*p < 0.05$, $**p < 0.01$.

(H) Correlation between $CD36^+$ foamy macrophages and bacterial burdens in brain during the neurolisteriosis. R, correlation coefficient.

(I) Immunofluorescence staining of $CD36^+$ foamy macrophages in cerebral vasculature of mice with neurolisteriosis. $CD36^+$ foamy macrophages were stained with CD11b (red) and CD36 (green). The boundary of vascular was depicted in dashed lines. Scale bar, 100 μm.

Abbreviations: PBMC, peripheral blood mononuclear cell; i.p., intraperitoneally; FMφ, foamy macrophages; CFU, colony forming units.

Figure 2. Infected foamy macrophages transfer bacteria into brain parenchyma *in vitro* and *in vivo*.

(A) Schematic diagram of an *in vitro* BBB model based on Transwell system.

(B) Quantification of bacterial burden in the macrophages penetrating into the lower

chamber of Transwell system under different concentrations of ox-LDL.

(C-D) (C) Representative image of macrophages that penetrated into the lower chamber. Scale bar, 100 μm. (D) Quantification of the penetrating cells in each field of view.

(E) Experimental diagram of adoptive macrophage transfer.

(F-I) After the adoptive macrophage transfer, recipient mice were intraperitoneally infected with 2×10^8 CFU *L. monocytogenes*. (F) Survival of recipient mice (n=10 for each group). (G-I) Bacterial burdens in brains (G), and cytokine levels in plasma (H) and brain homogenate (I) of recipient mice on day 1.25 (n=5 for each group).

(J-N) (J) Schematic diagram of adoptive macrophage transfer and infection experiments among $PCSK9^{+/+}$ (WT) and $PCSK9^{-/-}$ (KO) mice. Peritoneal macrophages from $PCSK9^{+/+}$ and $PCSK9^{-/-}$ mice were injected into $PCSK9^{+/+}$ and $PCSK9^{-/-}$ mice, respectively, followed by *L. monocytogenes* infection.

(K, M) Bacterial burdens in the brains of recipient mice after intraperitoneal injection (K) or oral administration (M) of *L. monocytogenes* (n=5 for each group).

(L, N) Survival of recipient mice after intraperitoneal injection (L) or oral administration (N) of *L. monocytogenes* (n=10 for each group).

Experiments were performed in duplicate (E-N) or triplicate (A-D). Data are presented as mean ± SEM. *$p < 0.05$, **$p < 0.01$. Abbreviations: ox-LDL, oxidized low density lipoprotein; FOV, field of view; NS, normal saline; PMφ, purified peritoneal macrophages; FMφ, $CD36^+$ foamy macrophages; i.p., intraperitoneally; ns, nonsignificant.

Figure. 3 Two-dimensional live-cell flow chamber assay of the migration characteristics of infected foamy macrophages.

(A) Schematic diagram of live-cell flow chamber experiment. Primary peritoneal macrophages were pretreated with ox-LDL for 24 hours and then infected with *L. monocytogenes* (MOI=10) for 6 hours.

(B-C) (B) Optical images of ox-LDL pretreated macrophages adhering to the surface of monolayer endothelial cells under shear flow. Scale bar, 200 μm. (C) Quantification of adherent cells in each field of view.

(D) Resistance to shear flow after adhesion of ox-LDL pretreated macrophages to endothelial cells. Upon 10-min adherence of equal macrophages to the monolayer endothelial cells at 1 dyn/cm^2, the shear stress was stepwise increased to 2, 4, 8, 16, and 32 dyn/cm^2 for 30 s sequentially to detach those adhered cells.

(E-H) Crawling dynamics of ox-LDL pretreated macrophages under shear flow. (E) Typical trajectories of ox-LDL pretreated macrophages crawling on monolayer endothelial cells. For each trajectory, the arrested sites of macrophages were overlaid at the origin of the diagram (x/y=0/0) and the corresponding end points were indicated with dots. Arrows indicate the flow direction. (F-H) Quantification of crawling displacement (F), velocity (G) and directness (H).

(I) Transmigration duration of ox-LDL pretreated macrophages after adhesion to the surface of monolayer endothelial cells.

(J-K) Quantification of the number (J) and mean length (K) of protrusions in ox-LDL

705 pretreated macrophages.

706 (L) Quantification of cell area in ox-LDL pretreated macrophages.

707 (M) qRT-PCR analysis of relative expression of genes associated with intercellular

708 adhesion molecules.

709 Experiments were performed in triplicate. Data are presented as mean ± SEM. *p <

710 0.05, **p < 0.01. Abbreviations: ox-LDL, oxidized low density lipoprotein.

711

712 **Figure 4. β-hydroxybutyrate aggravates bacterial neuroinvasion by promoting**

713 **the formation of CD36^{+} foamy macrophages via HCAR2 receptor.**

714 (A-C) Lipid metabolomic profiling analyses of serum from the mice with or without

715 neurolisteriosis. The mice of neurolisteriosis group were infected with 2×10^{8} CFU *L.*

716 *monocytogenes* for 24 hours (n=6 for each group). (A) Principal coordinates analysis

717 (PCA) analysis of differences between groups. (B) Expression of fatty acids (FAs) in

718 the serum was shown in the volcano plot. Differentially expressed FAs were selected

719 with |log2 fold change|>1 and adjusted P < 0.05. The dark blue dots represent down-

720 regulated FAs and the orange dots represent up-regulated FAs. (C) Classification of

721 the up-regulated FAs (SCFA, short chain fatty acids; MCFA, medium chain fatty acids;

722 LCFA, long chain fatty acids; VLCFA, very long chain fatty acids) shown in the pie

723 chart.

724 (D) Biochemical analysis of serum BHB levels in mice during the neurolisteriosis.

725 (E-Q) Primary peritoneal macrophages were extracted from 8-week-old HCAR2$^{+/+}$

726 and HCAR2$^{-/-}$ mice in preparation for further functional analysis. HCAR2$^{+/+}$ and

HCAR2$^{-/-}$ macrophages were pretreated with BHB (10 mM) for 24 hours and then infected with *L. monocytogenes* (MOI=10) for 6 hours.

(E-F) (E) Flow cytometry analysis of BODYPY FL 493/503 in BHB-treated macrophages (0, 5, 10 mM). (F) The histogram represents normalized MFI.

(G) Flow cytometry analysis of CD36^{+} foamy macrophages in BHB-treated macrophages (0, 5, 10 mM).

(H) Quantification of bacterial burden in the macrophages penetrating into the lower chamber of Transwell system. The macrophages stimulated with ox-LDL (80 ng/ml) were used as positive control.

(I-J) (I) Optical images of adherent macrophages on the surface of monolayer endothelial cells. Scale bar, 200 μm. (J) Quantification of adherent cells in each field of view.

(K) Resistance to shear flow after adhesion of macrophages to endothelial cells.

(L-P) Crawling and migrating dynamics of infected macrophages under shear flow. (L) Typical trajectories of infected macrophages crawling on monolayer endothelial cells. Quantification of crawling displacement (M), velocity (N), directness (O) and transmigration duration (P).

(Q) mRNA expression of intercellular α-integrin in infected macrophages.

Experiments were performed in duplicate (D) or triplicate (E-Q). Data are presented as mean ± SEM. *$p < 0.05$, **$p < 0.01$. Abbreviations: ns, nonsignificant; BHB, β-hydroxybutyrate; MFI, mean value of fluorescence intensity.

Figure 5. β-hydroxybutyrate promotes the survival of macrophage via HCAR2-mediated calcium influx.

(A-L) Primary peritoneal macrophages were extracted from 8-week-old HCAR2$^{+/+}$ and HCAR2$^{-/-}$ mice, cells were then infected with *L. monocytogenes* (MOI=10) for 6 hours.

(A-C) HCAR2$^{+/+}$ and HCAR2$^{-/-}$ macrophages were pretreated with BHB (10 mM) before infection. (A) Quantification of the percentage of released lactate dehydrogenase (LDH) in cell culture medium. (B) Immunofluorescence of Propylene glycol (PI)-stained macrophages. DAPI (blue) labels the nucleus and PI (red) labels the cell membrane. (C) Quantification of the percentage of PI^{+} cells after infection.

(D) Flow cytometry analysis of dynamics in intracellular calcium concentration. Infected macrophages were preloaded with Fluo-4 AM. BHB (10 mM) was added to the buffer after a span of 30 s.

(E-G) Macrophages were pretreated with BHB (10 mM) or BAPTA (10 mM) for 24 hours before infection. (E) Quantification of the percentage of released lactate dehydrogenase (LDH) in cell culture medium. (F) Quantification of the percentage of PI^{+} cells after infection. (G) Quantification of bacterial burden in the macrophages penetrating into the lower chamber of Transwell system.

(H-I) (H) Infected macrophages were treated with BHB (10 mM). Time-lapse images of CHMP4B-EGFP in macrophages were collected at 0, 5, 10, 15, 20, 30 min post BHB treatment with confocal microscopy. (I) Quantification of CHMP4B-EGFP puncta.

(J-L) HCAR2$^{+/+}$ and HCAR2$^{-/-}$ macrophages were pretreated with BHB (10 mM) for 24 hours before infection. (J) Flow cytometry analysis of LAMP1 expression on the cell surface. (K) The histogram representing normalized MFI. (L) Quantification of the lysosomal enzyme (acid phosphatase [ACP], β-galactosidase [β-gal] and β-hexosaminidase [β-hex]) activity released into the culture medium.

Experiments were performed in triplicate. Data are presented as mean ± SEM. *$p < 0.05$, **$p < 0.01$. Abbreviations: ns, nonsignificant; BHB, β-hydroxybutyrate.

Figure 6. Ketogenesis exacerbates neurolisteriosis through β-hydroxybutyrate-HCAR2 signaling.

(A-D) (A) Schematic diagram of *in vivo* KE supplementation. C57BL/6 mice were supplemented with KE (10, 20 mg/ml) in drinking water for 2 weeks and then challenged with 2×10^8 CFU *L. monocytogenes*. Serum BHB levels (B) and bacterial burdens in the parenchymal organs (D) were detected (n=5 for each group). (C) Survival of mice exposed *L. monocytogenes* (n=10 for each group).

(E-M) (E) Schematic diagram of *in vivo* ketogenic diet. HCAR2$^{+/+}$ and HCAR2$^{-/-}$ mice were treated with ketogenic or control diets, respectively, for 4 weeks, followed by intraperitoneal infection with 2×10^8 CFU *L. monocytogenes*. (F) Survival of mice exposed to *L. monocytogenes* (n=10 for each group). (G) Flow cytometry analysis of CD36$^+$ foamy macrophages before and after neurolisteriosis. (H-M) (H-I) Bacterial burdens in peripheral blood macrophages (H) and parenchymal organs (I) of mice on day 29. (J-K) Cytokine levels in the plasma (J) and brain homogenate (K). (L-M)

793 Representative Hematein & Eosin staining (L) and pathology scores (M) of cerebral
794 cortex tissue. Scale bar, 10 μm. (n=5 for each group).
795 Experiments were performed in duplicate. Data are presented as mean ± SEM. *p <
796 0.05, **p < 0.01. Abbreviations: ns, nonsignificant; KE, Ketone ester; CD, control
797 diet; KD, ketogenic diet; FMφ, foamy macrophages; i.p., intraperitoneally.
798
799 **Figure 7. Levels of β-hydroxybutyrate are decreased in bacterial meningitis in**
800 **humans, which correlated with the severity of disease.**
801 (A) Schematic diagram of HC (n=60) and BM (n=62) samples. The BM patients were
802 divided into three groups according to serum BHB levels.
803 (B) Serum BHB level in HC and BM patients.
804 (C-I) Clinical scores (C), cell counts (D) and protein levels (E) in cerebrospinal fluid,
805 white blood cells (WBC, F), procalcitonin (PCT, G), erythrocyte sedimentation rate
806 (ESR, H) and C-reactive protein (CRP, I) in BM patients with different BHB levels.
807 (J-K) Dynamics of $CD36^+$ foamy macrophages (J) and serum BHB (K) in 7 BM
808 donors after admission. The time after admission was divided into symptomatic and
809 convalescent periods according to clinical and laboratory indexes of infection. The
810 scatter plot on the right panel represents the statistics of AUC.
811 (L) Relative expression of genes involved in lipid metabolism in PBMCs from HC
812 and BM patients was detected by qRT-PCR.
813 Data are presented as mean ± SEM. *p < 0.05, **p < 0.01. Abbreviations: ns,
814 nonsignificant; HC, healthy control; BM, bacterial meningitis; AUC, area under the

curve; FMφ, foamy macrophages; BHB, β-hydroxybutyrate .

Figure S1. Additional results of identification of CD36$^+$foamy macrophage accumulation during the neurolisteriosis, related to Figure 1.

(A-B) C57BL/6 mice were intraperitoneally infected with 2×10^8 CFU *L. monocytogenes.* (A) Bacterial burdens in brains. (B) Survival of the mice (n=10 for each group). The yellow shading represents the range of confidence interval.

(C) Cell clusters identified in 10× scRNA-seq dataset. The top 10 enriched genes for each cluster are highlighted. Normalized z-score is used to illustrate gene expression.

(D) Proportion of each cluster according to experimental conditions in Figure 1D.

(E) Gating strategy for analysis of CD36$^+$ foamy macrophages in PBMCs.

(F) CD36$^+$ and CD36$^-$ macrophages were sorted from peripheral blood by flow cytometry and then stained with BODIPY FL 493/503 and oil Red O. Scale bar, 10 μm.

(G) Normalized intake of Dil-oxLDL by CD36$^+$ and CD36$^-$ macrophages.

Experiments were performed in duplicate (A-B) or triplicate (F-G). Data are presented as mean ± SEM. *$p < 0.05$, **$p < 0.01$. Abbreviations: FMφ, foamy macrophages.

Figure S2. Additional results of adoptive transfer of foamy macrophages *in vitro* and *in vivo*, related to Figure 2.

(A) Conversion of mice peritoneal macrophages into CD36$^+$ foamy macrophages by treating them with different concentrations of ox-LDL for 24 hours.

(B) Intracellular bacterial burden was quantified in macrophages challenged with *L. monocytogenes* (MOI=10) in the upper chamber of Transwell system under different concentrations of ox-LDL.

(C-G) The adoptive macrophage transfer experiment was shown in Figure 2E-2I (n=5 for each group). Recipient mice were intraperitoneally infected with 2×10^8 CFU *L. monocytogenes*. (C-D) Body weight changes (C) and clinical scores (D) of recipient mice during neurolisteriosis. (E) Bacterial burdens in other tissues (lung, spleen, liver) of recipient mice on day 1.25. (F-G) Representative Hematein & Eosin staining (F) and the pathology scoring (G) of cerebral cortex tissue. Scale bar, 20 μm.

(H-I) After adoptive macrophage transfer, recipient mice were intraperitoneally infected with 5×10^7 CFU *L. monocytogenes*. Bacterial burdens in brains (H) and other tissues (I) of recipient mice on day 1.25 were detected.

Experiments were performed in duplicate (C-I) or triplicate (A-B). Data are presented as mean ± SEM. *$p < 0.05$, **$p < 0.01$. Abbreviations: ns, nonsignificant; NS, normal saline; PMφ, purified peritoneal macrophages; FMφ, $CD36^+$ foamy macrophages; i.p., intraperitoneally.

Figure S3. Accumulation of $CD36^+$ foamy macrophages exacerbate intracellular bacteria neuroinvasion.

(A-F) Mice were intravenously infected with *S. Typhimurium* (A-B), MRSA (C-D) or *S. pneumoniae* (E-F), respectively (n=5 for each group). (A, C, E) Flow cytometry analysis of $CD36^+$ foamy macrophages during neuroinvasion. (B, D, F) Correlation

between $CD36^+$ foamy macrophages and bacterial burden in the brain during bacteria neuroinvasion. R, correlation coefficient.

(G-K) After the adoptive macrophage transfer, recipient mice were intraperitoneally infected with 2×10^8 CFU MRSA. (G) Survival of recipient mice (n=10 for each group). (H-I) Bacterial burdens in the brains (H) and other tissues (lung, spleen, liver). (J-K) Cytokine levels in plasma (J) and brain homogenate (K) of recipient mice on day 1.5 (n=5 for each group).

(L-O) Mice were intraperitoneally infected with 1×10^8 CFU *S. pneumoniae* (n=5 for each group). (L) Survival rate of mice (n=10). (M) Bacterial burdens in tissues. (N-O) Cytokine levels in plasma (N) and brain homogenate (O) of recipient mice on day 2 (n=5 for each group).

Experiments were performed in duplicate. Data are presented as mean ± SEM. *$p < 0.05$, **$p < 0.01$. Abbreviations: ns, nonsignificant.

Figure S4. Additional results of bidirectional transfer of macrophages from $PCSK9^{+/+}$ and $PCSK9^{-/-}$ mice, related to Figure 2.

(A-B) (A) Flow cytometry analysis of lipid droplets in peritoneal macrophages of $PCSK9^{+/+}$ and $PCSK9^{-/-}$ mice. (B) The histogram represents normalized MFI.

(C) Peritoneal macrophages of $PCSK9^{+/+}$ and $PCSK9^{-/-}$ mice were infected with *L. monocytogenes* (MOI=10) for 2 hours and then incubated in a fresh solution containing 5 μg/mL lysostaphin for 2 or 12 hours. Intracellular bacterial burden of infected macrophages was quantified

(D) Flow cytometry analysis of $CD36^+$ foamy macrophages during neurolisteriosis in $PCSK9^{+/+}$ and $PCSK9^{-/-}$ mice, respectively (n=5 for each group).

(E-G) Recipient mice in Figure 2J were intraperitoneally infected with 2×10^8 CFU *L. monocytogenes*. (E) Bacterial burdens in other tissues (lung, spleen, liver). (F-G) Cytokine levels in plasma (F) and brain homogenate (G) (n=5 for each group).

(H-J) Recipient mice in Figure 2J were orally infected with 2×10^8 CFU *L. monocytogenes*. (H) Bacterial burdens in other tissues (lung, spleen, liver). (I-J) Cytokine levels in plasma (I) and brain homogenate (J) (n=5 for each group).

Experiments were performed in duplicate (D-J) or triplicate (A-C). Data are presented as mean ± SEM. *$p < 0.05$, **$p < 0.01$. Abbreviations: ns, nonsignificant; i.p., intraperitoneally.

Figure S5. Supplemental data for the live-cell flow chamber assays, related to Figure 3.

(A-D) Optical images of *L. monocytogenes* infected macrophages (with or without ox-LDL stimulation) on the surface of endothelial monolayers with different densities (A) or endothelial monolayers derived from different tissues (C). Scale bar, 200 μm. (B, D) Quantification of adherent cells in each field of view.

(E) Schematic trajectory used for defining macrophage crawling parameters.

(F) Crawling duration of *L. monocytogene*-infected macrophages after adhesion to endothelial monolayer surface.

(G) Relative fluorescence intensity of a macrophage on endothelial surface over time.

It is a random example to illustrate the definition of transmigration duration. A 70% decrease in fluorescence intensity after a macrophage crosses a monolayer is considered successful transmigration.

Experiments were performed in triplicate. Data are presented as mean ± SEM. *$p < 0.05$, **$p < 0.01$. Abbreviations: CVEC, cerebrovascular endothelial cell; PVEC, pulmonary vascular endothelial cell; LSEC, liver sinusoidal endothelial cell; TEM, transendothelial migration; ns, nonsignificant.

Figure S6. Additional results from the influence of β-hydroxybutyrate on macrophages during neuroinvasion, related to Figure 4.

(A) KEGG enrichment analysis of lipid metabolites.

(B) Mass spectrometry analysis of serum BHB levels.

(C-D) Relative expression of the gene transcripts regulating ketogenesis in liver (HMGCS2, CPT1A) detected by qRT-PCR.

(E-F) Body weight changes (E) and food uptake (F) were monitored every 6 hours during neuroinvasion.

(G-H) Biochemical analysis of serum BHB levels in mice during neuroinvasion by *S. typhimurium* (G) and MRSA (H).

(I-J) $HCAR2^{+/+}$ and $HCAR2^{-/-}$ macrophages were pretreated with BHB (10 mM) and cAMP (1 mM) for 24 hours and then infected with *L. monocytogenes* (MOI=10) for 6 hours. Quantification of the normalized MFI of BODIPY FL 493/503 (I) and the bacterial burden in the macrophages penetrating into the lower chamber of Transwell

system (J).

Experiments were performed in duplicate (C-H) or triplicate (I-J). Data are presented as mean ± SEM. *p < 0.05, **p < 0.01. Abbreviations: ns, nonsignificant; MFI, mean fluorescence intensity.

Figure S7. Additional results on the role of β-hydroxybutyrate in regulating macrophage survival, related to Figure 5.

(A-F) Primary peritoneal macrophages were extracted and then infected with *L. monocytogenes* (MOI=10) for 6 hours.

(A) Macrophages were pretreated with BHB (10 mM) or BAPTA (10 mM) for 24 hours before infection. Intracellular bacterial burden of macrophages in the upper chamber of Transwell system was quantified.

(B-C) (B) Infected macrophages were treated with BHB (10 mM). Time-lapse images of CHMP4B-EGFP in macrophages were collected at 0, 5, 10, 15, 20, 30 min post BHB treatment with confocal microscopy. (C) Quantification of CHMP4B-EGFP puncta.

(D-F) Peritoneal macrophages were pretreated with BHB (10 mM) or BAPTA (10 mM) for 24 hours before infection. (D) Flow cytometry analysis of LAMP1 expression on the cell surface. (E) The histogram representing normalized MFI. (F) Quantification of the lysosomal enzyme activity released into the culture medium. Experiments were performed in triplicate. Data are presented as mean ± SEM. *p < 0.05, **p < 0.01. Abbreviations: ns, nonsignificant; BHB, β-hydroxybutyrate; MFI,

mean fluorescence intensity.

Figure S8. Additional results on the role of ketogenesis in bacterial neuroinvasion, related to Figure 6.

(A-B) The KE supplemental experiment was shown in Figure 6A-6D. (A) Flow cytometry analysis of $CD36^{+}$ foamy macrophages in mice supplemented with KE. (B) Clinical scores of mice supplemented with KE.

(C-D) The ketogenic diet experiment was shown in Figure 6E-6M. Body weight changes (C) and clinical scores (D) of mice during *L. monocytogenes* infection.

(E-H) $HCAR2^{+/+}$ and $HCAR2^{-/-}$ mice were treated with ketogenic and control diets, respectively, for 4 weeks, followed by oral infection with 2×10^{8} CFU *L. monocytogenes*. (E) Survival of mice exposed to *L. monocytogenes* (n=10 for each group). (F) Bacterial burdens in organs (brain, lung, spleen, liver). Cytokine levels in plasma (G) and brain homogenate (H) (n=5 for each group).

(I-K) C57BL/6 mice were treated with ketogenic and control diets, respectively, for 4 weeks, followed by intravenous infection with 2×10^{8} CFU MRSA. (I) Survival of mice exposed to MRSA (n=15 for each group). (J) Bacterial burdens in organs (brain, lung, spleen, liver). (K) Clinical scores of mice during neuroinvasion (n=5 for each group).

Experiments were performed in duplicate. Data are presented as mean ± SEM. $^{*}p < 0.05$, $^{**}p < 0.01$. Abbreviations: ns, nonsignificant; i.p., intraperitoneally.

Figure S9. Additional results of high levels of BHB and human tuberculous meningitis, related to Figure 7.

(A-D) Glucose (A) and insulin (C) levels in serum from HC and BM patients. Correlation between serum glucose level and BHB (B), as well as serum insulin levels and BHB (D) in BM patients. R, correlation coefficient

(E-F) Serum triglyceride (TC, E), high density lipoprotein (HDL-C, F) and low density lipoprotein (LDL-C, G) from HC and BM patients.

Data are presented as mean ± SEM. *$p < 0.05$, **$p < 0.01$. Abbreviations: ns, nonsignificant, HC, health control, BM, bacterial meningitis.

EXPERIMENTAL MODEL AND STUDY PARTICIPANT DETAILS

Clinical samples

Bacterial meningitis (BM) disease subjects (n = 62, 32 males and 30 females, aged 41.62 ±15.68 years) and healthy donors (n = 60, 30 males and 30 females, aged 38.32±9.17 years) were recruited from Chongqing Public Health Medical Center. Isolation of PBMCs and single-cell suspensions was performed using PBMC Isolation Kit (P8680, Solarbio) by density gradient centrifugation. Plasma was collected from each patient and donor and then used for quantification of BHB. This study was carried out in strict accordance with the Guidelines for the Care and Use of Animals of Chongqing University, and was compliant with the “Guidance of the Ministry of Science and Technology (MOST) for the Review and Approval of Human Genetic

Resources". Healthy individuals and patients providing blood samples were given informed consent. The ethics committee approved this consent procedure. The clinical symptoms of the BM patients included burnout, headache, irritability, vomiting, fever, neck stiffness, convulsion, and consciousness disorder. Each symptom is worth 1 point.

Animal

All animal experiments were performed following institutional guidelines at Chongqing University. In all experiments, control and experimental mice were 6-8-week-old littermates of male C57BL/6 mice. Littermates of the same sex were housed together regardless of genotype. All mice were maintained under a 12-hour light-dark cycle with ad libitum access to regular food and water.

Bacterial strains

L. monocytogenes (19115) and *S. pneumoniae* 49619 were grown in Brain Heart Infusion Broth. Methicillin-resistant *Staphylococcus aureus* USA300 and *S. Typhimurium* were grown in Luria-Bertani Broth.

Data and code availability

Single-cell RNA-seq data have been deposited at GEO and are publicly available as of the date of publication.

1013 **METHOD DETAILS**

1014 **Single cell RNA-sequencing analysis**

1015 Isolated PBMCs from the mice were transported in in sterile culture dish with 10 ml
1016 Dulbecco's Phosphate-Buffered Saline (DPBS, Thermo Fisher Scientific) on ice to
1017 remove the residual tissue storage solution, then minced on ice. We used dissociation
1018 enzyme 0.25% Trypsin (Thermo Fisher Scientific) and 10 ug/mL DNase I (Sigma)
1019 dissolved in PBS with 5% Fetal Bovine Serum (FBS, GIBCO) to digest the tissues.
1020 PBMCs were dissociated at 37 ℃ under a shaking speed of 50 rpm for about 40 min.
1021 We repeatedly collected the dissociated cells at interval of 20 min to increase cell
1022 yield and viability. Cell suspensions were filtered using a 40-μm nylon cell strainer
1023 and red blood cells were removed by red blood cell lysis solution (Thermo Fisher
1024 Scientific). Dissociated cells were washed with DPBS containing 2% FBS.
1025 10× beads were then subject to second-strand cDNA synthesis, adaptor ligation, and
1026 universal amplification. Sequencing libraries were prepared using randomly
1027 interrupted whole-transcriptome amplification products to enrich the 3' end of the
1028 transcripts linked with the cell barcode and UMI. All the remaining procedures
1029 including the library construction were performed according to the standard
1030 manufacturer's protocol (Chromium Single Cell 3' v3). Sequencing libraries were
1031 quantified using a High Sensitivity DNA Chip (Agilent) on a Bioanalyzer 2100 and
1032 the Qubit High Sensitivity DNA Assay (Thermo Fisher Scientific). The libraries were
1033 sequenced on NovaSeq6000 (Illumina) using 2×150 chemistry. The sequencing and
1034 bioinformatic analysis were performed on platform of Majorbio Co., Ltd (Shanghai,

China).

Reads were processed using the Cell Ranger (v7.1.0) pipeline with default and recommended parameters. FASTQs generated from Illumina sequencing output were aligned to the mouse genome, version GRCm38, using the STAR algorithm. Gene-barcode matrix containing the barcoded cells and gene expression counts were generated. This output was then imported into the Seurat (v3.2.0) R toolkit for quality control and downstream analysis of our single cell RNAseq data.

Cells were clustered using graph-based clustering of the PCA reduced data with the Louvain Method after computing a shared nearest neighbor graph. For sub-clustering, we applied the same procedure of scaled, dimensionality reduction, and clustering to the specific set of data. For each cluster, we used the Wilcoxon Rank-Sum Test to find significant deferentially expressed genes comparing to the remaining clusters.

To identify differential expression genes (DEGs) between two different samples or clusters, was performed using the function FindMarkers in Seurat, using a likelihood ratio test. Essentially, DEGs with $|\log2FC| > 0.25$ and Q value $\leqslant 0.05$ were significantly different expressed genes. In addition, functional-enrichment analysis GO were performed to identify which DEGs were significantly enriched in GO terms and metabolic pathways at Bonferroni-corrected P-value $\leqslant$ 0.05 compared with the whole-transcriptome background. GO functional enrichment analysis were carried out by Goatools (https://github.com/tanghaibao/Goatools).

Mouse model of acute bacteria brain neuroinvasion

Mice were challenged with pathogenic bacteria (2×10^8 CFU *L. monocytogenes* or MRSA, 1×10^8 CFU *S. Typhimurium* or *S. pneumoniae*) and weighed and scored every 3 hours. The progression of acute bacterial meningitis was determined by clinical scores as previously described with a few adaptations.[65] Clinical scoring was performed based on the Table S2, including activity (0–2), time to return to upright position (0–2), eyes (0–2) and neurological examination (0–2). Mice were deeply anaesthetized by an intraperitoneal injection of tribromoethanol solution (Avertin, 500 mg/kg) and transcranial perfused with saline solution for brain tissue pathomorphology. Blood was sampled immediately before perfusion. Tissue samples, including brain, lung, liver, and spleen, were dissected and weighed.

Analysis Bacterial load in cell or tissue

Tissue samples of mice were transferred into 2 ml tubes containing 4 mm stainless steel beads (Qiagen) and 1 ml of ice-cold sterile saline. Homogenization was carried out in TissueLyser II (Qiagen) for 5 min at 70 Hz. Serial dilutions of the homogenates were plated on the plates incubated at 37℃ and CFU were counted.

The infected macrophages were incubated in a fresh solution containing 5 μg/mL lysostaphin for the indicated periods and then lysed by 0.2% Triton to release intracellular bacteria. The lysates were diluted to appropriate dilutions with sterile PBS for CFU count on agar plates.

Brain histopathology and Immunostaining

1079 Brain samples were collected from infected mice 24 hours after injection. Mice were
1080 deeply anaesthetized with tribromoethanol solution (Avertin, 500 mg/kg,
1081 intravenously) and transcranial perfused with 30 ml saline solution followed by 10 ml
1082 of 4% Paraformaldehyde (PFA) in saline. After dissection, brain samples were
1083 maintained in 4% PFA at 4 ℃. Fixed brains were embedded in paraffin, sectioned and
1084 half of the slides were stained using haematoxylin and eosin. Each field was assigned
1085 a score from 0 to 3 based on neuronal morphology: grade 0 (not altered); grade 1 (no
1086 vacuolation with small numbers of pyknotic cells); grade 2 (moderate vacuolation and
1087 pyknosis); and grade 3 (extensive vacuolation, pyknosis and tissue loss or liquefactive
1088 necrosis).
1089 Fresh frozen brain tissue sections of 5-10 mm thickness were mounted on slides, air
1090 dried for 10 minutes at room temperature and fixed in ice cold 10% neutral-buffered
1091 formalin for 5-10 min. Slices were washed in PBS, then incubated for 2 hours in 3%
1092 bovine serum albumin (BSA) and then 0.1% Triton X-100 in PBS. The slides were
1093 labelled with the appropriate primary antibodies of CD11b and CD36 overnight at 4 ℃
1094 in mild blocking conditions. Next day, the slices were washed in PBS, and then
1095 incubated with secondary antibodies and DAPI. Tissues were washed in PBS and then
1096 mounted on glass slides under coverslips in mounting medium. The slides were left in
1097 darkness overnight before observation under a Zeiss LSM900 or LM710 microscope.
1098

1099 **Cell sorting and flow cytometry.**

1100 Isolated mouse PBMCs were cleaned twice with PBS. After calculating and

1101 determining the appropriate concentration, appropriate amount of fluorescent-coupled
1102 primary antibody (F4/80-APC, CD11b-FITC, as the marker of macrophage, CD36-
1103 FITC) was added respectively. Incubate at 4 ℃ for 30 min away from light. The
1104 living macrophages were collected according to the expression of CD36 and then
1105 culture in vitro overnight. The sorting cells were detected the lipid content using
1106 BODIPY FL and oil Red O. To evaluate the ability of lipid uptake, macrophages were
1107 incubated with 40 μg/ml DiI-ox-LDL particles for 6h and then detect the fluorescence
1108 intensity by flow cytometry.
1109 To determine the proportion of foamy macrophages population, cells were stained
1110 with fluorescent-coupled primary antibody (F4/80-APC, CD11b-PE, CD36-FITC) at
1111 4 ℃ for 30 min away from light. To detect the expression of LAMP1 on the cell
1112 surface, infected macrophages were cleaned twice with PBS and then stained with
1113 LAMP1-FITC at 4 ℃ for 30 min away from light. The cells were washed three times
1114 and then re-suspended in 200μl of the staining buffer for final FACS analysis. Data
1115 was analyzed with FlowJo software.
1116
1117 **Isolation and culture of primary cells**
1118 To generate peritoneal macrophages, 8-week-old mice were injected intraperitoneally
1119 with 3% thioglycolate broth. After 72 hours, peritoneal cells were harvested, and
1120 macrophages were enriched by quick adherence.
1121 Primary endothelial cells were isolated from 8 to 12-week-old male C57BL/6 mice.
1122 The cerebral cortex in the brains were separated and rolled on the filter paper to

remove the meninges and choroid plexuses. A mechanical reduction was performed by mincing the brain pieces using surgical blades. The homogenate was centrifuged (800 g, 8 min, 4℃) and the precipitate was digested in DMEM containing 1 mg/ml type II collagenase and 58.5 U/ml type I DNase for 75 min on a benchtop orbital shaker at 37 ℃. The supernatant was finally collected and centrifuged at 500 g for 8 min. The isolated cerebrovascular endothelial cells were purified by the anchoring technique. The liver and lung from an anaesthetized mouse were perfused via the portal vein sequentially with balanced salt solution containing 5 mM glucose, 0.01% sodium heparin, and 5 mM EGTA and high glucose DMEM medium containing 4 mM $CaCl_2$, 2% FBS and 0.05% collagenase IV (Sigma-Aldrich, St. Louis, MO) at a flow rate of 5 ml/min for 5 min, respectively. The following steps are similar in order to separate the liver sinusoids endothelial cells and pulmonary vascular endothelial cells.

Isolation of primary embryonic neurons and single-cell suspensions was performed using Pierce Primary Neuron Isolation Kit (88280, Thermo Scientific) by density gradient centrifugation.

In vitro blood-brain barrier

The *in vitro* BBB model was constructed with primary endothelial cells using a Transwell cell culture system. Briefly, CVECs were seeded onto the upper chamber of the Transwell pre-coated with gelatine, and cultured with the medium containing 10% FBS. The integrity of the monolayer cell was evaluated by measuring the TEER

values using a Millicell-ERS voltohmmeter (Millipore). The cell monolayers with TEER values higher than 300 Ω.cm^2 were used as the BBB model for the transmigration studies. The neurons cells were seeded onto the lower chamber of the Transwell for bacterial load.

Macrophages were exposed to *L. monocytogenes* (MOI=10) for 6 hours. After the BBB model has been constructed, the infected macrophages were digested for cell counting and added into the upper chamber. The conventional incubation time was 12 hours and then the neurons cells in the bottom chamber were lysed for penetrating bacterial quantification.

Adoptive macrophages transfer in mouse bacteria brain neuroinvasion

Peritoneal macrophages from donor mice were collected via intraperitoneal injection of thioglycolate. Following further cultivation, purified macrophages were obtained. To collect CD36$^+$ foamy macrophages, purified macrophages were stimulated with 80 μg/ml ox-LDL over 24 hours. Recipient mice were pretreated with 3 days of CTX and then intraperitoneally given 0.2 ml normal saline or cell suspension (1×10^6 per mouse) on Day 0. After adoptive macrophages transfer, recipient mice were intraperitoneally injected with 2×10^8 CFU of *L. monocytogenes* in 12 hours and euthanized after 18 hours.

Purified peritoneal macrophages were harvested from PCSK9$^{+/+}$ and PCSK9$^{-/-}$ donor mice respectively, and then transferred to recipient mice as depicted in Figure 2J. Recipient mice were infected with 2×10^8 CFU *L. monocytogenes* 12 hours after

macrophages transfer and euthanized after 24 hours.

Live-cell flow chamber assay

A flow cell system was used to test macrophages adhesion, shear resistance, crawling, and transmigration, on endothelial monolayer, which was performed as previously described.[42] Shear flow was applied by a syringe pump (PHD22/2000, Harvard Apparatus) into a microfluidic chip with a 100 μm × 1 mm× 15 mm main flowing zone. Different shear stresses were acquired by setting corresponding volumetric flow rates. Isolated macrophages were stimulated under different concentration of ox-LDL for 24 hours and then infected with *L. monocytogenes* (MOI=10) for 6 hours. Macrophages were re-suspended and stained with Hoechst. The cells were then perfused over pre-formed endothelial monolayer for 8 min at a shear stress of 0.1 dyne/cm^2. Then, the adhesion and crawling dynamics of macrophages on endothelial monolayer was recorded at 2 dyn/cm^2 for 10 min at 20× objective by a CCD camera. Images were taken from the video every second and analyzed the crawling parameters and transmigrating duration with Image J software. Here a macrophage crossing the monolayer with a 70% fluorescence intensity reduction was deemed transmigrated. For testing shear-resistant macrophage adhesion, primed macrophages were re-suspended and counted. The same number of cells (2×10^4) were completely perfused over pre-formed endothelial monolayer within 10 min. The shear stress was increased stepwise from 1 to 2, 4, 8, 16, 32 dyn/cm^2 for 30s each. Remaining adherent macrophages on endothelial monolayer were recorded at 20× objective by a CCD

camera and counted using Image J software. The normalized adhesion fraction was calculated by dividing the number of adherent macrophages at the endpoint of each shear phase by the number at the endpoint of 1 dyn/cm^2. For defining the macrophage transmigration dynamics, the time-lapse images were analyzed offline frame-by-frame every second.

Quantification of *L. monocytogenes* protrusion formation

Isolated peritoneal macrophages were stimulated under different concentration of ox-LDL for 24 hours and then infected with CFSE-labeled *L. monocytogenes* (MOI=10) for 6 hours. At 4 hours post-infection, cells were fixed, permeabilized, and labeled with mouse anti-ezrin and phalloidin-Alexa 647. Samples were analyzed using confocal microscopy. Protrusions were identified as bacteria with ezrin tails that project from host cells into neighboring. In each experiment, ten cells were scored for each condition. The lengths of ezrin comet tails were measured using ImageJ software.

Lipid metabolomics

Metabolite extraction and mass spectrometry detection was processed using Ultra-High Performance Liquid Chromatography-mass spectrometry (UHPLC-MS) of Biomarker Technologies (Beijing, China). The raw data collected using MassLynx V4.2 is processed by Progenesis QI software for peak extraction, peak alignment, and other data processing operations, based on the Progenesis QI software online METLIN database and Biomark's self-built library for identification. The theoretical

1211 fragment identification and mass deviation are within 100 ppm. After normalizing the
1212 original peak area information with the total peak area, the follow-up analysis was
1213 performed. Principal component analysis (PCA) and Spearman correlation analysis
1214 were used to judge the repeatability of the samples within group and the quantity
1215 control samples. The identified compounds are searched for classification and
1216 pathway information in KEGG and HMDB databases.
1217 A total of 4,625 named metabolites were retained for datasets. The R language
1218 package ropls was used to perform OPLS-DA modeling, and 200 times permutation
1219 tests was performed to verify the reliability of the model. The screening criteria are
1220 FC>1, $p < 0.05$ and VIP>1. The difference metabolites of KEGG pathway enrichment
1221 significance were calculated using hypergeometric distribution test.
1222
1223 **Fura-4 Ca^{2+} imaging**
1224 Cells were removed from incubator and washed with PBS and then incubated with 5
1225 μM Fluo-4 AM (Beyotime) for 60 min at 37 ℃ with 0.04% Pluronic-127. After
1226 incubation, cells were washed with PBS and incubated with PBS for 30 min at 37 ℃.
1227 Fluorescence were detected with a CytoFLEX Flow Cytometer (Beckman Coulter)
1228 equipped with 488 nm excitation wavelength. As indicated, BHB (10 mM) were
1229 added into the cells pre-loaded with Fluo-4 30 s after the record. Data was analyzed
1230 with Flow Jo to determine the fluorescence intensity.
1231
1232 **Diets for *in vivo* assays**

1233 When indicated, mice were administered a supplement of 20 mg/ml ketone ester (D-
1234 β-hydroxybutyrate-(R)-1,3 butanediol monoester) in the drinking water for 4 weeks
1235 before the infection. Ketogenic diets (# XTKD01, Xietong Pharma Co.) contained 10%
1236 protein and 90% fat while the control diets contained 23.2% protein, 2.8% fat and 74%
1237 sugar. Mice were consequently placed on either the ketogenic or control diet for an
1238 additional 4 weeks before infection.
1239

1240 **Real-time qRT-PCR**

1241 Total RNA was isolated using an RNeasy Mini Kit (QIAGEN). The mRNA was
1242 reverse-transcribed and quantified using a HiScript II 1st Strand cDNA Synthesis Kit
1243 (Vazyme). qRT-PCR was performed on an ABI StepOnePlus PCR system (Thermo
1244 Fisher Scientific), and results were normalized to GAPDH mRNA levels. Data were
1245 analyzed using the 2-DDct method.
1246

1247 **QUANTIFICATION AND STATISTICAL ANALYSIS**

1248 Statistical analysis was performed using GraphPad Prism Software. Two-group
1249 comparisons were made using two-tailed unpaired Student's t-test. One-way analysis
1250 of variance (ANOVA) with appropriate multiple comparisons tests was used to
1251 compare three independent groups. For comparisons of multiple factors, two-way
1252 ANOVA with appropriate multiple comparisons tests was used. Exact *p* values for
1253 specific group comparisons in all the figures. A value of $p < 0.05$ was considered
1254 significant. Specific details of statistical analysis are presented above or in associated

figure legends.

Reference

1. Doran, K.S., Fulde, M., Gratz, N., Kim, B.J., Nau, R., Prasadarao, N., Schubert-Unkmeir, A., Tuomanen, E.I., and Valentin-Weigand, P. (2016). Host-pathogen interactions in bacterial meningitis. Acta Neuropathol *131*, 185-209. 10.1007/s00401-015-1531-z.
2. Hasbun, R. (2022). Progress and Challenges in Bacterial Meningitis: A Review. JAMA *328*, 2147-2154. 10.1001/jama.2022.20521.
3. Rua, R., and McGavern, D.B. (2018). Advances in Meningeal Immunity. Trends Mol Med *24*, 542-559. 10.1016/j.molmed.2018.04.003.
4. Merlini, A., Haberl, M., Strauss, J., Hildebrand, L., Genc, N., Franz, J., Chilov, D., Alitalo, K., Flugel-Koch, C., Stadelmann, C., et al. (2022). Distinct roles of the meningeal layers in CNS autoimmunity. Nat Neurosci *25*, 887-899. 10.1038/s41593-022-01108-3.
5. Byrd, T.F., and Davis, L.E. (2007). Multidrug-resistant tuberculous meningitis. Curr Neurol Neurosci Rep *7*, 470-475. 10.1007/s11910-007-0073-8.
6. Huynh, J., Donovan, J., Phu, N.H., Nghia, H.D.T., Thuong, N.T.T., and Thwaites, G.E. (2022). Tuberculous meningitis: progress and remaining questions. Lancet Neurol *21*, 450-464. 10.1016/S1474-4422(21)00435-X.
7. van de Beek, D., Brouwer, M.C., Koedel, U., and Wall, E.C. (2021). Community-acquired bacterial meningitis. Lancet *398*, 1171-1183.

10.1016/S0140-6736(21)00883-7.

8. Levin, B.R., Baquero, F., Ankomah, P.P., and McCall, I.C. (2017). Phagocytes, Antibiotics, and Self-Limiting Bacterial Infections. Trends Microbiol *25*, 878-892. 10.1016/j.tim.2017.07.005.

9. Boada-Romero, E., Martinez, J., Heckmann, B.L., and Green, D.R. (2020). The clearance of dead cells by efferocytosis. Nat Rev Mol Cell Biol *21*, 398-414. 10.1038/s41580-020-0232-1.

10. Locati, M., Curtale, G., and Mantovani, A. (2020). Diversity, Mechanisms, and Significance of Macrophage Plasticity. Annu Rev Pathol *15*, 123-147. 10.1146/annurev-pathmechdis-012418-012718.

11. Zhai, L., Huang, C., Ning, Z., Zhang, Y., Zhuang, M., Yang, W., Wang, X., Wang, J., Zhang, L., Xiao, H., et al. (2023). Ruminococcus gnavus plays a pathogenic role in diarrhea-predominant irritable bowel syndrome by increasing serotonin biosynthesis. Cell Host Microbe *31*, 33-44 e35. 10.1016/j.chom.2022.11.006.

12. Van der Merwe, S., Chokshi, S., Bernsmeier, C., and Albillos, A. (2021). The multifactorial mechanisms of bacterial infection in decompensated cirrhosis. J Hepatol *75 Suppl 1*, S82-S100. 10.1016/j.jhep.2020.11.029.

13. Maudet, C., Kheloufi, M., Levallois, S., Gaillard, J., Huang, L., Gaultier, C., Tsai, Y.H., Disson, O., and Lecuit, M. (2022). Bacterial inhibition of Fas-mediated killing promotes neuroinvasion and persistence. Nature *603*, 900-906. 10.1038/s41586-022-04505-7.

14. Xu, K., Yin, N., Peng, M., Stamatiades, E.G., Shyu, A., Li, P., Zhang, X., Do, M.H., Wang, Z., Capistrano, K.J., et al. (2021). Glycolysis fuels phosphoinositide 3-kinase signaling to bolster T cell immunity. Science *371*, 405-410. 10.1126/science.abb2683.

15. Escoll, P., Song, O.R., Viana, F., Steiner, B., Lagache, T., Olivo-Marin, J.C., Impens, F., Brodin, P., Hilbi, H., and Buchrieser, C. (2017). Legionella pneumophila Modulates Mitochondrial Dynamics to Trigger Metabolic Repurposing of Infected Macrophages. Cell Host Microbe *22*, 302-316 e307. 10.1016/j.chom.2017.07.020.

16. Yang, D., Jacobson, A., Meerschaert, K.A., Sifakis, J.J., Wu, M., Chen, X., Yang, T., Zhou, Y., Anekal, P.V., Rucker, R.A., et al. (2022). Nociceptor neurons direct goblet cells via a CGRP-RAMP1 axis to drive mucus production and gut barrier protection. Cell *185*, 4190-4205 e4125. 10.1016/j.cell.2022.09.024.

17. Loft, A., Schmidt, S.F., Caratti, G., Stifel, U., Havelund, J., Sekar, R., Kwon, Y., Sulaj, A., Chow, K.K., Alfaro, A.J., et al. (2022). A macrophage-hepatocyte glucocorticoid receptor axis coordinates fasting ketogenesis. Cell Metab *34*, 473-486 e479. 10.1016/j.cmet.2022.01.004.

18. Puchalska, P., and Crawford, P.A. (2017). Multi-dimensional Roles of Ketone Bodies in Fuel Metabolism, Signaling, and Therapeutics. Cell Metab *25*, 262-284. 10.1016/j.cmet.2016.12.022.

19. Tomlinson, K.L., Chen, Y.T., Junker, A., Urso, A., Wong Fok Lung, T., Ahn,

D., Hofstaedter, C.E., Baskota, S.U., Ernst, R.K., Prince, A., and Riquelme, S.A. (2023). Ketogenesis promotes tolerance to Pseudomonas aeruginosa pulmonary infection. Cell Metab *35*, 1767-1781 e1766. 10.1016/j.cmet.2023.09.001.

20. Goldberg, E.L., Molony, R.D., Kudo, E., Sidorov, S., Kong, Y., Dixit, V.D., and Iwasaki, A. (2019). Ketogenic diet activates protective gammadelta T cell responses against influenza virus infection. Sci Immunol *4*. 10.1126/sciimmunol.aav2026.

21. Seufert, A.L., Hickman, J.W., Traxler, S.K., Peterson, R.M., Waugh, T.A., Lashley, S.J., Shulzhenko, N., Napier, R.J., and Napier, B.A. (2022). Enriched dietary saturated fatty acids induce trained immunity via ceramide production that enhances severity of endotoxemia and clearance of infection. Elife *11*. 10.7554/eLife.76744.

22. Wilhelm, C., Surendar, J., and Karagiannis, F. (2021). Enemy or ally? Fasting as an essential regulator of immune responses. Trends Immunol *42*, 389-400. 10.1016/j.it.2021.03.007.

23. Singh, V., Jamwal, S., Jain, R., Verma, P., Gokhale, R., and Rao, K.V. (2012). Mycobacterium tuberculosis-driven targeted recalibration of macrophage lipid homeostasis promotes the foamy phenotype. Cell Host Microbe *12*, 669-681. 10.1016/j.chom.2012.09.012.

24. McFarland, A.P., Yalin, A., Wang, S.Y., Cortez, V.S., Landsberger, T., Sudan, R., Peng, V., Miller, H.L., Ricci, B., David, E., et al. (2021). Multi-tissue

single-cell analysis deconstructs the complex programs of mouse natural killer and type 1 innate lymphoid cells in tissues and circulation. Immunity *54*, 1320-1337 e1324. 10.1016/j.immuni.2021.03.024.

25. Ahmad, F., Rani, A., Alam, A., Zarin, S., Pandey, S., Singh, H., Hasnain, S.E., and Ehtesham, N.Z. (2022). Macrophage: A Cell With Many Faces and Functions in Tuberculosis. Front Immunol *13*, 747799. 10.3389/fimmu.2022.747799.

26. Hill, D.A., Lim, H.W., Kim, Y.H., Ho, W.Y., Foong, Y.H., Nelson, V.L., Nguyen, H.C.B., Chegireddy, K., Kim, J., Habertheuer, A., et al. (2018). Distinct macrophage populations direct inflammatory versus physiological changes in adipose tissue. Proc Natl Acad Sci U S A *115*, E5096-E5105. 10.1073/pnas.1802611115.

27. Jaitin, D.A., Adlung, L., Thaiss, C.A., Weiner, A., Li, B., Descamps, H., Lundgren, P., Bleriot, C., Liu, Z., Deczkowska, A., et al. (2019). Lipid-Associated Macrophages Control Metabolic Homeostasis in a Trem2-Dependent Manner. Cell *178*, 686-698 e614. 10.1016/j.cell.2019.05.054.

28. Luis, G., Godfroid, A., Nishiumi, S., Cimino, J., Blacher, S., Maquoi, E., Wery, C., Collignon, A., Longuespee, R., Montero-Ruiz, L., et al. (2021). Tumor resistance to ferroptosis driven by Stearoyl-CoA Desaturase-1 (SCD1) in cancer cells and Fatty Acid Biding Protein-4 (FABP4) in tumor microenvironment promote tumor recurrence. Redox Biol *43*, 102006. 10.1016/j.redox.2021.102006.

29. Victor, M.B., Leary, N., Luna, X., Meharena, H.S., Scannail, A.N., Bozzelli, P.L., Samaan, G., Murdock, M.H., von Maydell, D., Effenberger, A.H., et al. (2022). Lipid accumulation induced by APOE4 impairs microglial surveillance of neuronal-network activity. Cell Stem Cell *29*, 1197-1212 e1198. 10.1016/j.stem.2022.07.005.

30. Xu, S., Chaudhary, O., Rodriguez-Morales, P., Sun, X., Chen, D., Zappasodi, R., Xu, Z., Pinto, A.F.M., Williams, A., Schulze, I., et al. (2021). Uptake of oxidized lipids by the scavenger receptor CD36 promotes lipid peroxidation and dysfunction in CD8(+) T cells in tumors. Immunity *54*, 1561-1577 e1567. 10.1016/j.immuni.2021.05.003.

31. Guerrini, V., and Gennaro, M.L. (2019). Foam Cells: One Size Doesn't Fit All. Trends Immunol *40*, 1163-1179. 10.1016/j.it.2019.10.002.

32. Luo, Y., Duan, H., Qian, Y., Feng, L., Wu, Z., Wang, F., Feng, J., Yang, D., Qin, Z., and Yan, X. (2017). Macrophagic CD146 promotes foam cell formation and retention during atherosclerosis. Cell Res *27*, 352-372. 10.1038/cr.2017.8.

33. Kim, K., Shim, D., Lee, J.S., Zaitsev, K., Williams, J.W., Kim, K.W., Jang, M.Y., Seok Jang, H., Yun, T.J., Lee, S.H., et al. (2018). Transcriptome Analysis Reveals Nonfoamy Rather Than Foamy Plaque Macrophages Are Proinflammatory in Atherosclerotic Murine Models. Circ Res *123*, 1127-1142. 10.1161/CIRCRESAHA.118.312804.

34. Botham, K.M., and Wheeler-Jones, C.P. (2013). Postprandial lipoproteins and the molecular regulation of vascular homeostasis. Prog Lipid Res *52*, 446-464.

10.1016/j.plipres.2013.06.001.

35. Jaggi, U., Matundan, H.H., Yu, J., Hirose, S., Mueller, M., Wormley, F.L., Jr., and Ghiasi, H. (2021). Essential role of M1 macrophages in blocking cytokine storm and pathology associated with murine HSV-1 infection. PLoS Pathog *17*, e1009999. 10.1371/journal.ppat.1009999.

36. Pasula, R., Martin, W.J., 2nd, Kesavalu, B.R., Abdalla, M.Y., and Britigan, B.E. (2017). Passive transfer of interferon-gamma over-expressing macrophages enhances resistance of SCID mice to Mycobacterium tuberculosis infection. Cytokine *95*, 70-79. 10.1016/j.cyto.2017.02.009.

37. Peyrusson, F., Varet, H., Nguyen, T.K., Legendre, R., Sismeiro, O., Coppee, J.Y., Wolz, C., Tenson, T., and Van Bambeke, F. (2020). Intracellular Staphylococcus aureus persisters upon antibiotic exposure. Nat Commun *11*, 2200. 10.1038/s41467-020-15966-7.

38. Ding, Z., Pothineni, N.V.K., Goel, A., Luscher, T.F., and Mehta, J.L. (2020). PCSK9 and inflammation: role of shear stress, pro-inflammatory cytokines, and LOX-1. Cardiovasc Res *116*, 908-915. 10.1093/cvr/cvz313.

39. Da Dalt, L., Castiglioni, L., Baragetti, A., Audano, M., Svecla, M., Bonacina, F., Pedretti, S., Uboldi, P., Benzoni, P., Giannetti, F., et al. (2021). PCSK9 deficiency rewires heart metabolism and drives heart failure with preserved ejection fraction. Eur Heart J *42*, 3078-3090. 10.1093/eurheartj/ehab431.

40. Katsuki, S., P, K.J., Lupieri, A., Nakano, T., Passos, L.S.A., Rogers, M.A., Becker-Greene, D., Le, T.D., Decano, J.L., Ho Lee, L., et al. (2022).

Proprotein Convertase Subtilisin/Kexin 9 (PCSK9) Promotes Macrophage Activation via LDL Receptor-Independent Mechanisms. Circ Res *131*, 873-889. 10.1161/CIRCRESAHA.121.320056.

41. Qi, Z., Hu, L., Zhang, J., Yang, W., Liu, X., Jia, D., Yao, Z., Chang, L., Pan, G., Zhong, H., et al. (2021). PCSK9 (Proprotein Convertase Subtilisin/Kexin 9) Enhances Platelet Activation, Thrombosis, and Myocardial Infarct Expansion by Binding to Platelet CD36. Circulation *143*, 45-61. 10.1161/CIRCULATIONAHA.120.046290.

42. Yang, H., Li, N., Du, Y., Tong, C., Lu, S., Hu, J., Zhang, Y., and Long, M. (2017). Neutrophil adhesion and crawling dynamics on liver sinusoidal endothelial cells under shear flow. Exp Cell Res *351*, 91-99. 10.1016/j.yexcr.2017.01.002.

43. Neupane, A.S., Willson, M., Chojnacki, A.K., Vargas, E.S.C.F., Morehouse, C., Carestia, A., Keller, A.E., Peiseler, M., DiGiandomenico, A., Kelly, M.M., et al. (2020). Patrolling Alveolar Macrophages Conceal Bacteria from the Immune System to Maintain Homeostasis. Cell *183*, 110-125 e111. 10.1016/j.cell.2020.08.020.

44. Hernandez, G.E., and Iruela-Arispe, M.L. (2020). The many flavors of monocyte/macrophage--endothelial cell interactions. Curr Opin Hematol *27*, 181-189. 10.1097/MOH.0000000000000573.

45. Pang, X., He, X., Qiu, Z., Zhang, H., Xie, R., Liu, Z., Gu, Y., Zhao, N., Xiang, Q., and Cui, Y. (2023). Targeting integrin pathways: mechanisms and advances

in therapy. Signal Transduct Target Ther *8*, 1. 10.1038/s41392-022-01259-6.

46. Deng, L., Kersten, S., and Stienstra, R. (2023). Triacylglycerol uptake and handling by macrophages: From fatty acids to lipoproteins. Prog Lipid Res *92*, 101250. 10.1016/j.plipres.2023.101250.

47. Patterson, M.T., Firulyova, M.M., Xu, Y., Hillman, H., Bishop, C., Zhu, A., Hickok, G.H., Schrank, P.R., Ronayne, C.E., Caillot, Z., et al. (2023). Trem2 promotes foamy macrophage lipid uptake and survival in atherosclerosis. Nature Cardiovascular Research *2*, 1015-1031. 10.1038/s44161-023-00354-3.

48. Andrews, N.W., and Corrotte, M. (2018). Plasma membrane repair. Curr Biol *28*, R392-R397. 10.1016/j.cub.2017.12.034.

49. Jimenez, A.J., Maiuri, P., Lafaurie-Janvore, J., Divoux, S., Piel, M., and Perez, F. (2014). ESCRT machinery is required for plasma membrane repair. Science *343*, 1247136. 10.1126/science.1247136.

50. Newman, J.C., and Verdin, E. (2017). beta-Hydroxybutyrate: A Signaling Metabolite. Annu Rev Nutr *37*, 51-76. 10.1146/annurev-nutr-071816-064916.

51. Youm, Y.H., Nguyen, K.Y., Grant, R.W., Goldberg, E.L., Bodogai, M., Kim, D., D'Agostino, D., Planavsky, N., Lupfer, C., Kanneganti, T.D., et al. (2015). The ketone metabolite beta-hydroxybutyrate blocks NLRP3 inflammasome-mediated inflammatory disease. Nat Med *21*, 263-269. 10.1038/nm.3804.

52. Duking, T., Spieth, L., Berghoff, S.A., Piepkorn, L., Schmidke, A.M., Mitkovski, M., Kannaiyan, N., Hosang, L., Scholz, P., Shaib, A.H., et al. (2022). Ketogenic diet uncovers differential metabolic plasticity of brain cells.

Sci Adv *8*, eabo7639. 10.1126/sciadv.abo7639.

53. Lu, J.F., Zhu, M.Q., Xia, B., Zhang, N.N., Liu, X.P., Liu, H., Zhang, R.X., Xiao, J.Y., Yang, H., Zhang, Y.Q., et al. (2023). GDF15 is a major determinant of ketogenic diet-induced weight loss. Cell Metab *35*, 2165-2182 e2167. 10.1016/j.cmet.2023.11.003.

54. Matsuura, T.R., Puchalska, P., Crawford, P.A., and Kelly, D.P. (2023). Ketones and the Heart: Metabolic Principles and Therapeutic Implications. Circ Res *132*, 882-898. 10.1161/CIRCRESAHA.123.321872.

55. Shah, U.A., and Iyengar, N.M. (2022). Plant-Based and Ketogenic Diets As Diverging Paths to Address Cancer: A Review. JAMA Oncol *8*, 1201-1208. 10.1001/jamaoncol.2022.1769.

56. Iovino, F., Engelen-Lee, J.Y., Brouwer, M., van de Beek, D., van der Ende, A., Valls Seron, M., Mellroth, P., Muschiol, S., Bergstrand, J., Widengren, J., and Henriques-Normark, B. (2017). pIgR and PECAM-1 bind to pneumococcal adhesins RrgA and PspC mediating bacterial brain invasion. J Exp Med *214*, 1619-1630. 10.1084/jem.20161668.

57. Liu, Y., Li, J.Y., Chen, S.T., Huang, H.R., and Cai, H. (2016). The rLrp of Mycobacterium tuberculosis inhibits proinflammatory cytokine production and downregulates APC function in mouse macrophages via a TLR2-mediated PI3K/Akt pathway activation-dependent mechanism. Cell Mol Immunol *13*, 729-746. 10.1038/cmi.2015.58.

58. Steeb, B., Claudi, B., Burton, N.A., Tienz, P., Schmidt, A., Farhan, H., Maze,

A., and Bumann, D. (2013). Parallel exploitation of diverse host nutrients enhances Salmonella virulence. PLoS Pathog *9*, e1003301. 10.1371/journal.ppat.1003301.

59. Jiang, L., Wang, P., Song, X., Zhang, H., Ma, S., Wang, J., Li, W., Lv, R., Liu, X., Ma, S., et al. (2021). Salmonella Typhimurium reprograms macrophage metabolism via T3SS effector SopE2 to promote intracellular replication and virulence. Nat Commun *12*, 879. 10.1038/s41467-021-21186-4.

60. Allahverdian, S., Chaabane, C., Boukais, K., Francis, G.A., and Bochaton-Piallat, M.L. (2018). Smooth muscle cell fate and plasticity in atherosclerosis. Cardiovasc Res *114*, 540-550. 10.1093/cvr/cvy022.

61. Robichaud, S., Rasheed, A., Pietrangelo, A., Doyoung Kim, A., Boucher, D.M., Emerton, C., Vijithakumar, V., Gharibeh, L., Fairman, G., Mak, E., et al. (2022). Autophagy Is Differentially Regulated in Leukocyte and Nonleukocyte Foam Cells During Atherosclerosis. Circ Res *130*, 831-847. 10.1161/CIRCRESAHA.121.320047.

62. Boven, L.A., Van Meurs, M., Van Zwam, M., Wierenga-Wolf, A., Hintzen, R.Q., Boot, R.G., Aerts, J.M., Amor, S., Nieuwenhuis, E.E., and Laman, J.D. (2006). Myelin-laden macrophages are anti-inflammatory, consistent with foam cells in multiple sclerosis. Brain *129*, 517-526. 10.1093/brain/awh707.

63. Peyron, P., Vaubourgeix, J., Poquet, Y., Levillain, F., Botanch, C., Bardou, F., Daffe, M., Emile, J.F., Marchou, B., Cardona, P.J., et al. (2008). Foamy macrophages from tuberculous patients' granulomas constitute a nutrient-rich

reservoir for M. tuberculosis persistence. PLoS Pathog *4*, e1000204. 10.1371/journal.ppat.1000204.

64. Weis, E.M., Puchalska, P., Nelson, A.B., Taylor, J., Moll, I., Hasan, S.S., Dewenter, M., Hagenmuller, M., Fleming, T., Poschet, G., et al. (2022). Ketone body oxidation increases cardiac endothelial cell proliferation. EMBO Mol Med *14*, e14753. 10.15252/emmm.202114753.

65. Koopmans, M.M., Engelen-Lee, J., Brouwer, M.C., Jaspers, V., Man, W.K., Vall Seron, M., and van de Beek, D. (2018). Characterization of a Listeria monocytogenes meningitis mouse model. J Neuroinflammation *15*, 257. 10.1186/s12974-018-1293-3.

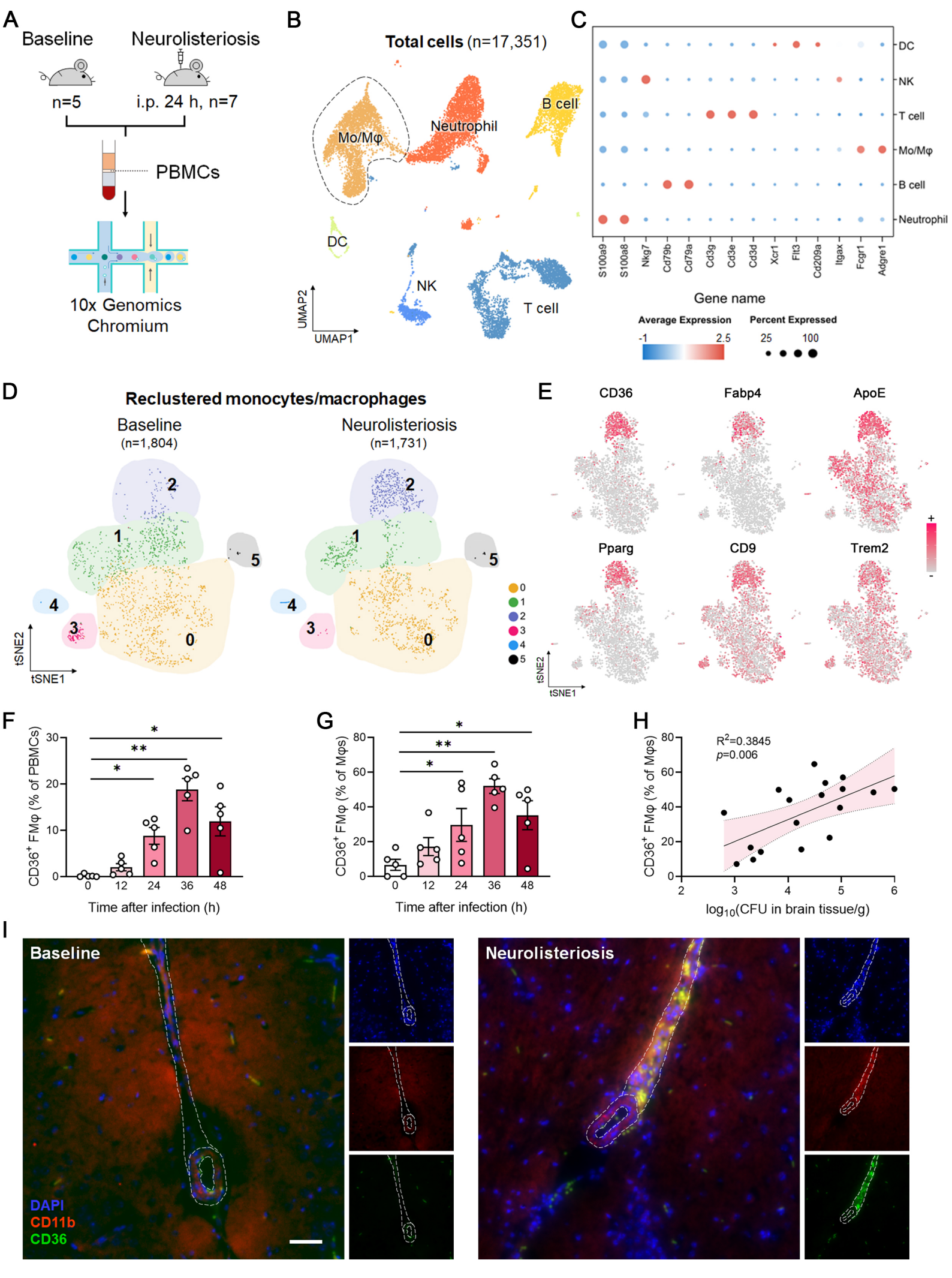
A
Baseline
Neurolisteriosis
n=5
i.p. 24 h, n=7
PBMCs
10x Genomics
Chromium
B
Total cells (n=17,351)
Mo/Mφ
Neutrophil
B cell
DC
NK
T cell
UMAP2
UMAP1
C
DC
NK
T cell
Mo/Mφ
B cell
Neutrophil
S100a9
S100a8
Nkg7
Cd79b
Cd79a
Cd3g
Cd3e
Cd3d
Xcr1
Flt3
Cd209a
Itgax
Fcgr1
Adgre1
Gene name
Average Expression
-1
2.5
Percent Expressed
25
100
D
Reclustered monocytes/macrophages
Baseline
(n=1,804)
Neurolisteriosis
(n=1,731)
tSNE2
tSNE1
E
CD36
Fabp4
ApoE
Pparg
CD9
Trem2
F
CD36+ FMφ (% of PBMCs)
Time after infection (h)
G
CD36+ FMφ (% of Mφs)
Time after infection (h)
H
R2=0.3845
p=0.006
CD36+ FMφ (% of Mφs)
log10(CFU in brain tissue/g)
I
Baseline
Neurolisteriosis
DAPI
CD11b
CD36

Figure 1

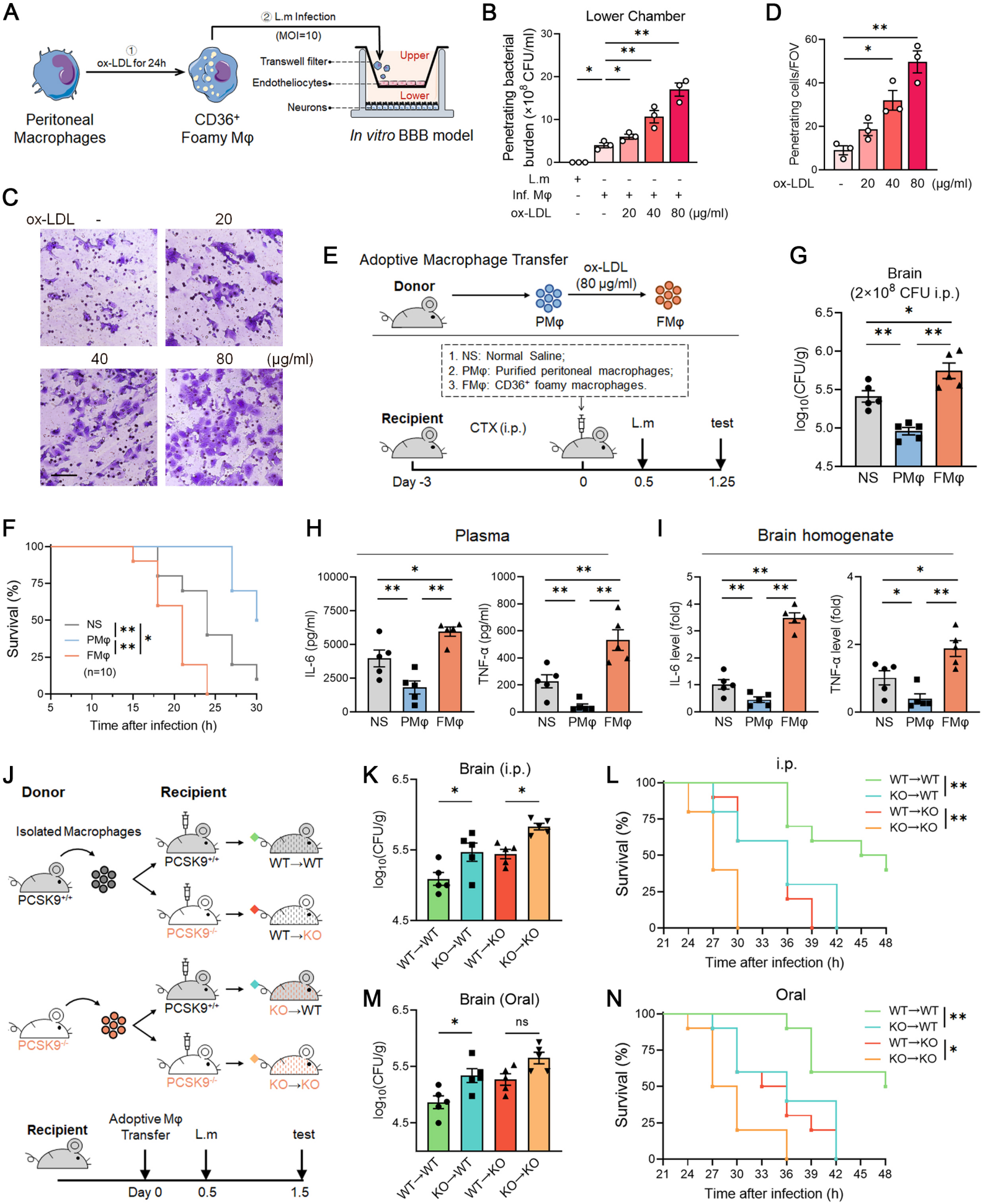
A
① ox-LDL for 24h
② L.m Infection (MOI=10)
Peritoneal Macrophages
CD36⁺ Foamy Mφ
Transwell filter
Endotheliocytes
Neurons
Upper
Lower
In vitro BBB model
B
Lower Chamber
Penetrating bacterial burden (×10⁸ CFU/ml)
L.m
Inf. Mφ
ox-LDL
80 (μg/ml)
D
Penetrating cells/FOV
ox-LDL
80 (μg/ml)
C
ox-LDL
20
40
80 (μg/ml)
E
Adoptive Macrophage Transfer
Donor
ox-LDL (80 μg/ml)
PMφ
FMφ
1. NS: Normal Saline;
2. PMφ: Purified peritoneal macrophages;
3. FMφ: CD36⁺ foamy macrophages.
Recipient
CTX (i.p.)
L.m
test
Day -3
0
0.5
1.25
G
Brain (2×10⁸ CFU i.p.)
log10(CFU/g)
NS
PMφ
FMφ
F
Survival (%)
NS
PMφ
FMφ
(n=10)
Time after infection (h)
H
Plasma
IL-6 (pg/ml)
TNF-α (pg/ml)
I
Brain homogenate
IL-6 level (fold)
TNF-α level (fold)
J
Donor
Recipient
Isolated Macrophages
PCSK9⁺⁺
PCSK9⁻⁻
WT→WT
WT→KO
KO→WT
KO→KO
Adoptive Mφ Transfer
L.m
test
Day 0
0.5
1.5
K
Brain (i.p.)
L
i.p.
WT→WT
KO→WT
WT→KO
KO→KO
Time after infection (h)
M
Brain (Oral)
ns
N
Oral

Figure 2

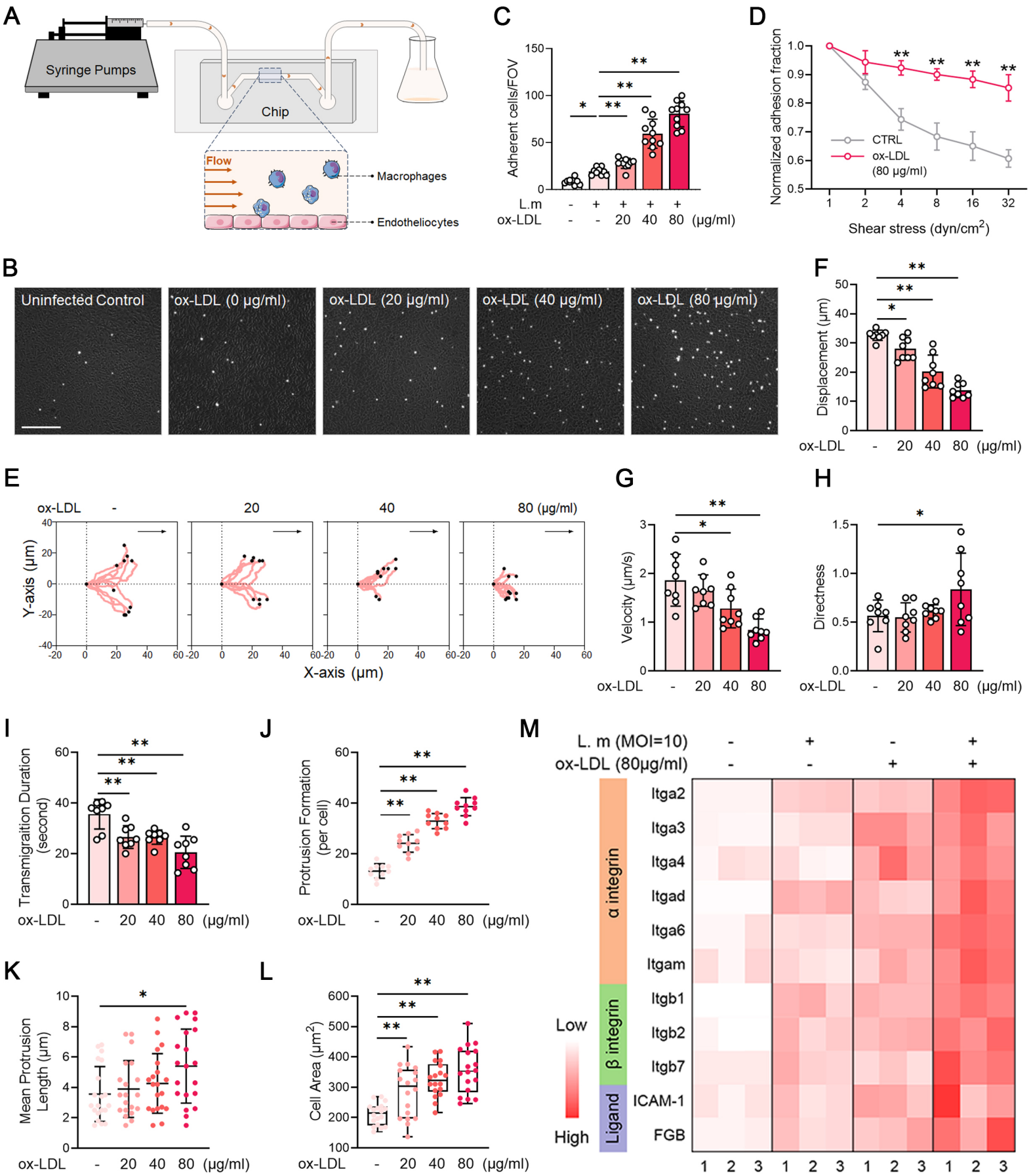
A
Syringe Pumps
Chip
Flow
Macrophages
Endotheliocytes
C
Adherent cells/FOV
L.m
ox-LDL
(μg/ml)
D
Normalized adhesion fraction
CTRL
ox-LDL
(80 μg/ml)
Shear stress (dyn/cm2)
B
Uninfected Control
ox-LDL (0 μg/ml)
ox-LDL (20 μg/ml)
ox-LDL (40 μg/ml)
ox-LDL (80 μg/ml)
F
Displacement (μm)
E
Y-axis (μm)
X-axis (μm)
G
Velocity (μm/s)
H
Directness
I
Transmigraition Duration (second)
J
Protrusion Formation (per cell)
K
Mean Protrusion Length (μm)
L
Cell Area (μm2)
M
L. m (MOI=10)
ox-LDL (80μg/ml)
α integrin
β integrin
Ligand
Itga2
Itga3
Itga4
Itgad
Itga6
Itgam
Itgb1
Itgb2
Itgb7
ICAM-1
FGB
Low
High

Figure 3

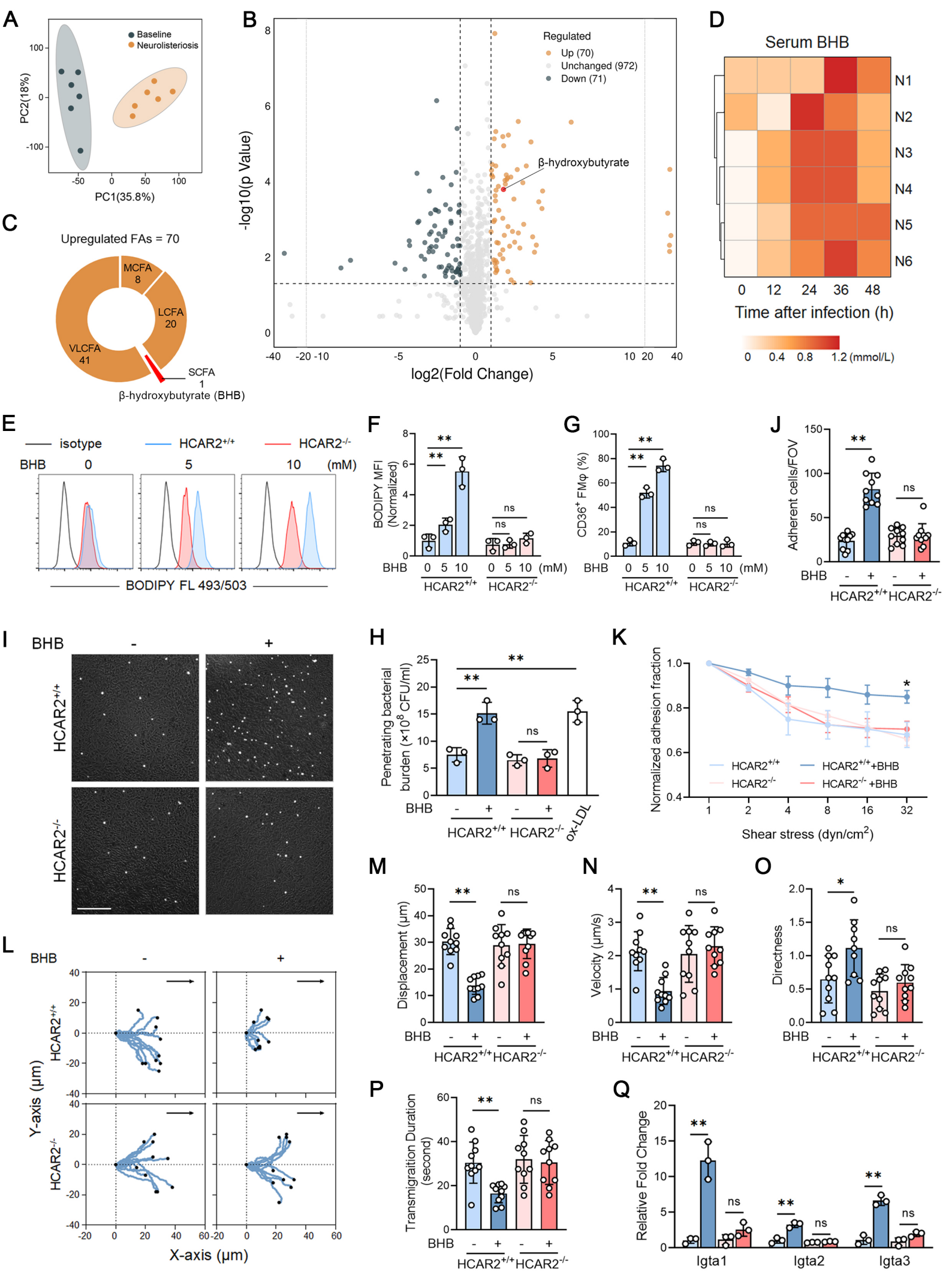
A
Baseline
Neurolisteriosis
PC2(18%)
PC1(35.8%)
B
Regulated
Up (70)
Unchanged (972)
Down (71)
β-hydroxybutyrate
-log10(p Value)
log2(Fold Change)
C
Upregulated FAs = 70
MCFA 8
LCFA 20
VLCFA 41
SCFA 1
β-hydroxybutyrate (BHB)
D
Serum BHB
N1
N2
N3
N4
N5
N6
Time after infection (h)
(mmol/L)
E
isotype
HCAR2+/+
HCAR2-/-
BHB
(mM)
BODIPY FL 493/503
F
BODIPY MFI (Normalized)
G
CD36+ FMφ (%)
J
Adherent cells/FOV
I
BHB
HCAR2+/+
HCAR2-/-
H
Penetrating bacterial burden (×10^8 CFU/ml)
ox-LDL
K
Normalized adhesion fraction
HCAR2+/+
HCAR2-/-
HCAR2+/+ +BHB
HCAR2-/- +BHB
Shear stress (dyn/cm2)
L
Y-axis (μm)
X-axis (μm)
M
Displacement (μm)
N
Velocity (μm/s)
O
Directness
P
Transmigraition Duration (second)
Q
Relative Fold Change
Igta1
Igta2
Igta3

Figure 4

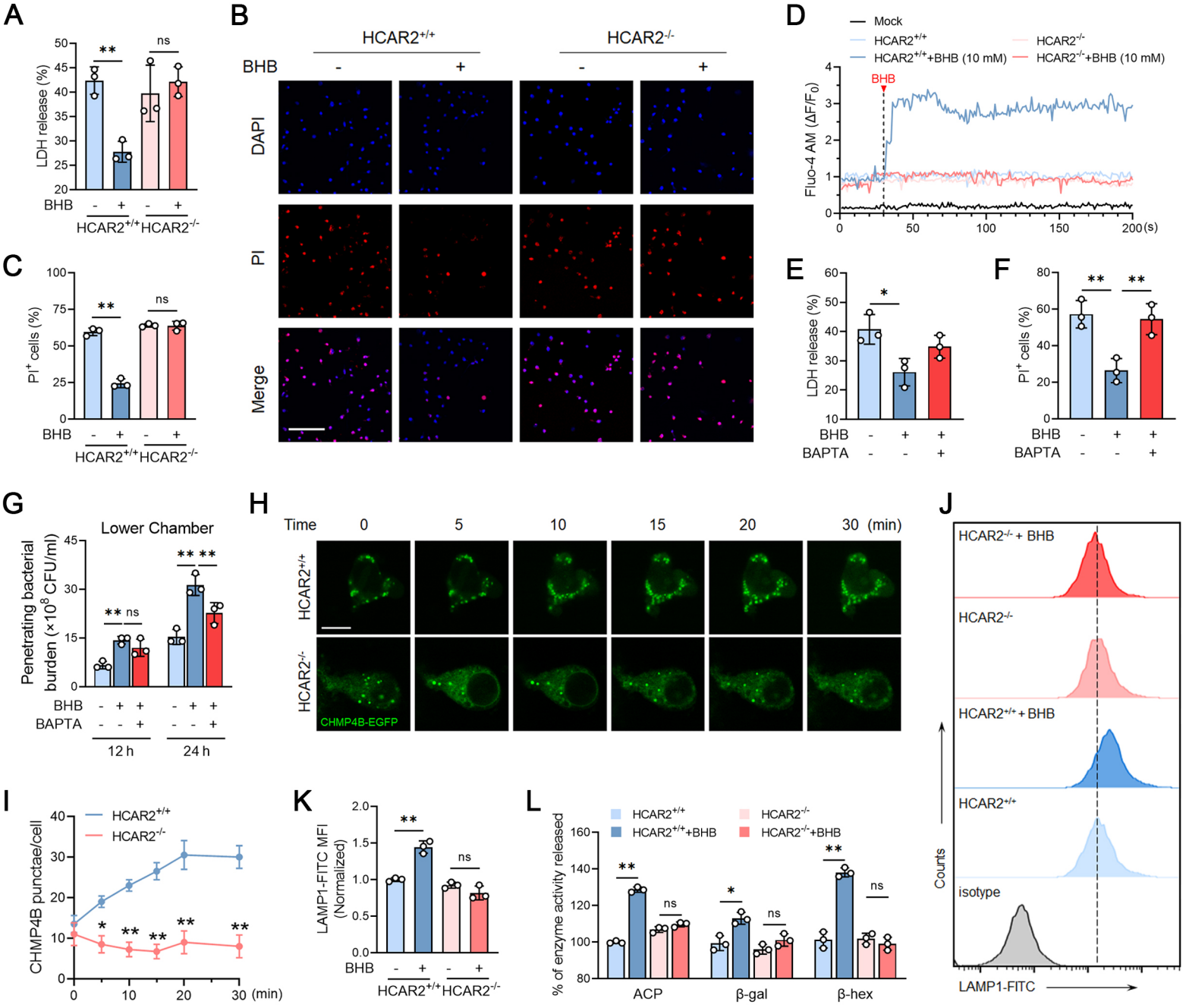
A
LDH release (%)
BHB
HCAR2+/+ HCAR2-/-
B
HCAR2+/+
HCAR2-/-
BHB
DAPI
PI
Merge
C
PI+ cells (%)
D
Mock
HCAR2+/+
HCAR2+/+ +BHB (10 mM)
HCAR2-/-
HCAR2-/- +BHB (10 mM)
BHB
Fluo-4 AM (ΔF/F0)
(s)
E
LDH release (%)
BAPTA
F
PI+ cells (%)
G
Lower Chamber
Penetrating bacterial burden (×10^8 CFU/ml)
12 h
24 h
H
Time
0
5
10
15
20
30 (min)
HCAR2+/+
HCAR2-/-
CHMP4B-EGFP
I
CHMP4B punctae/cell
(min)
J
HCAR2-/- + BHB
HCAR2-/-
HCAR2+/+ + BHB
HCAR2+/+
isotype
Counts
LAMP1-FITC
K
LAMP1-FITC MFI (Normalized)
L
HCAR2+/+
HCAR2+/+ +BHB
HCAR2-/-
HCAR2-/- +BHB
% of enzyme activity released
ACP
β-gal
β-hex

Figure 5

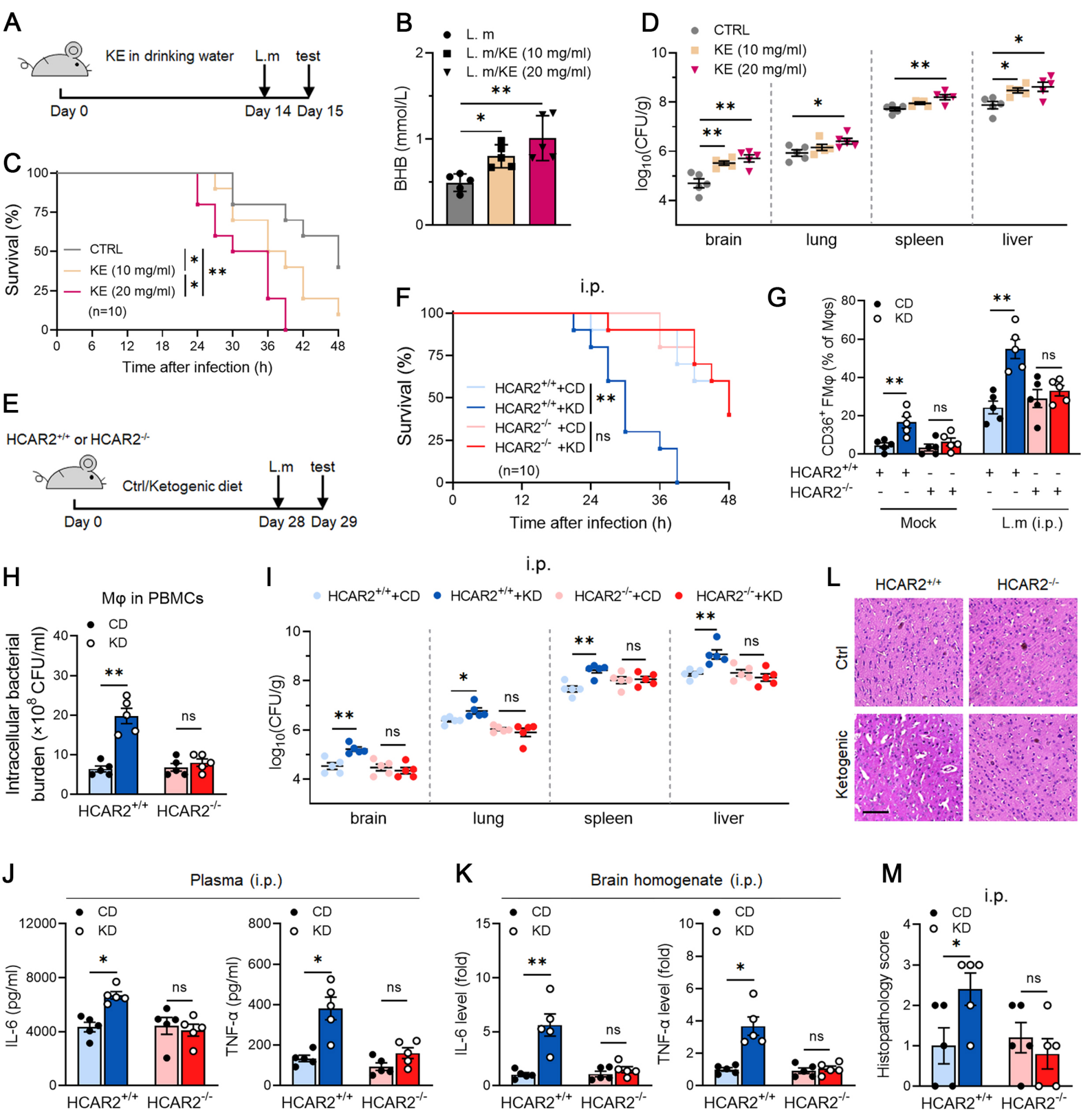
A
KE in drinking water
L.m
test
Day 0
Day 14
Day 15
B
L. m
L. m/KE (10 mg/ml)
L. m/KE (20 mg/ml)
BHB (mmol/L)
D
CTRL
KE (10 mg/ml)
KE (20 mg/ml)
log10(CFU/g)
brain
lung
spleen
liver
C
Survival (%)
CTRL
KE (10 mg/ml)
KE (20 mg/ml)
(n=10)
Time after infection (h)
E
HCAR2+/+ or HCAR2-/-
Ctrl/Ketogenic diet
L.m
test
Day 0
Day 28
Day 29
F
i.p.
Survival (%)
HCAR2+/++CD
HCAR2+/++KD
HCAR2-/- +CD
HCAR2-/- +KD
(n=10)
Time after infection (h)
G
CD
KD
CD36+ FMφ (% of Mφs)
HCAR2+/+
HCAR2-/-
Mock
L.m (i.p.)
H
Mφ in PBMCs
CD
KD
Intracellular bacterial burden (×10^8 CFU/ml)
HCAR2+/+
HCAR2-/-
I
i.p.
HCAR2+/++CD
HCAR2+/++KD
HCAR2-/-+CD
HCAR2-/-+KD
log10(CFU/g)
brain
lung
spleen
liver
L
HCAR2+/+
HCAR2-/-
Ctrl
Ketogenic
J
Plasma (i.p.)
CD
KD
IL-6 (pg/ml)
TNF-α (pg/ml)
HCAR2+/+
HCAR2-/-
K
Brain homogenate (i.p.)
CD
KD
IL-6 level (fold)
TNF-α level (fold)
HCAR2+/+
HCAR2-/-
M
i.p.
CD
KD
Histopathology score
HCAR2+/+
HCAR2-/-

Figure 6

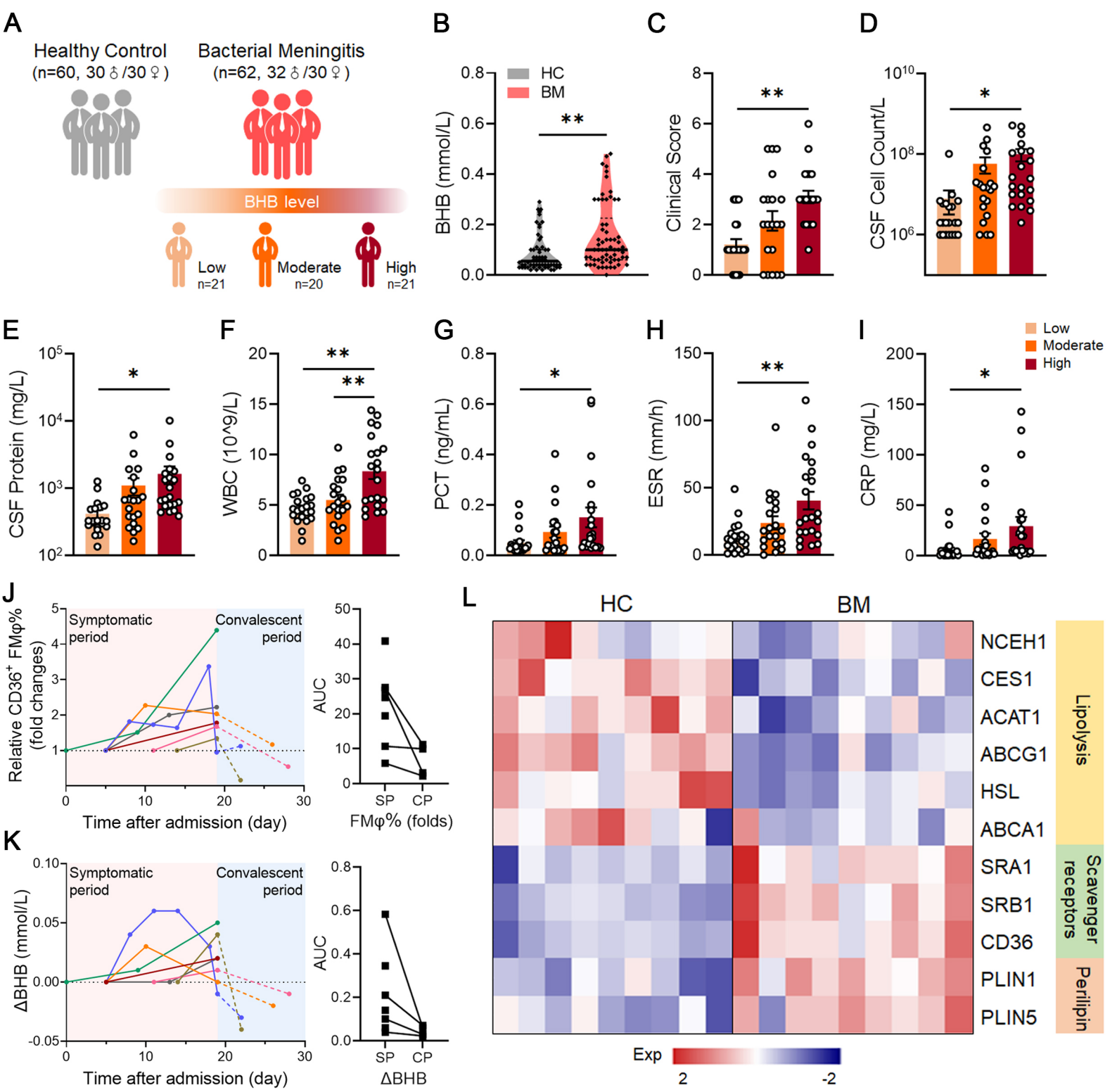
A
Healthy Control
(n=60, 30♂/30♀)
Bacterial Meningitis
(n=62, 32♂/30♀)
BHB level
Low
n=21
Moderate
n=20
High
n=21
B
HC
BM
BHB (mmol/L)
C
Clinical Score
D
CSF Cell Count/L
E
CSF Protein (mg/L)
F
WBC (10^9/L)
G
PCT (ng/mL)
H
ESR (mm/h)
I
CRP (mg/L)
Low
Moderate
High
J
Relative CD36+ FMφ%
(fold changes)
Symptomatic
period
Convalescent
period
Time after admission (day)
AUC
SP
CP
FMφ% (folds)
K
ΔBHB (mmol/L)
ΔBHB
L
HC
BM
NCEH1
CES1
ACAT1
ABCG1
HSL
ABCA1
SRA1
SRB1
CD36
PLIN1
PLIN5
Lipolysis
Scavenger receptors
Perilipin
Exp
2
-2

Figure 7